

PROCEEDINGS A

rspa.royalsocietypublishing.org



Article submitted to journal

Subject Areas:

Applied mathematics

Keywords:

Bifurcation, soft tubes, localised bulging, necking, two-phase deformation

Author for correspondence:

Dominic Emery

e-mail: d.r.emery@keele.ac.uk

Post-bifurcation behaviour of elasto-capillary necking and bulging in soft tubes

 Dominic Emery¹ and Yibin Fu¹

¹ School of Computing and Mathematics, Keele University, Staffordshire ST5 5BG, U.K.

An axially stretched soft cylindrical tube may develop an infinite-wavelength instability when one or both of its lateral surfaces are under sufficient surface tension. For fixed surface tension and increasing axial stretch, this instability occurs when the resultant axial force attains a maximum, though for fixed axial stretch and increasing surface tension, no such interpretation exists. A weakly non-linear analysis is conducted for a general material model to determine the explicit nature of this instability for multiple loading scenarios. The bifurcation solution is found to be localised bulging or necking depending on whether the axial stretch is greater or less than a certain threshold value at the point of bifurcation. At this threshold value, an exceptionally super-critical kink wave solution arises in place of localisation. By drawing upon previous Finite Element Method (FEM) simulations, and experimental findings for the analogous problem of tubes under internal inflation, a thorough interpretation of the anticipated post-bifurcation behaviour is given with the view to aiding future experimental studies of the problem at hand.

1. Introduction

A surge of interest in the behaviour, functionality and development of micro and nano-scale soft materials has transpired in recent years, with applications in soft robotics [1] and the construction of artificial muscles [2] and other biomedical devices [3] being at the forefront of this new-found motivation. A bi-product of this is the emerging field of *elasto-capillarity*, which is concerned with the finite deformation of elastic solids with surface energy [4–9]. This surface energy becomes non-negligible when the typical length scale of a system is comparable to the ratio of the surface tension γ to the ground state shear modulus μ [10]. Thus, when modelling extremely soft materials such as gels, elastomer's and biological tissue

© The Authors. Published by the Royal Society under the terms of the Creative Commons Attribution License <http://creativecommons.org/licenses/by/4.0/>, which permits unrestricted use, provided the original author and source are credited.

on the nano to milli-scale, the consideration of elasto-capillary effects is of vital importance. A geometry which arguably requires greater attention is the cylindrical tube, which is widespread in physiological systems in the form of arteries, airways and intestines, for instance. The villification of the gastrointestinal tract [11], the closure of pulmonary airways [12] and the gyrification of the brain [13] are examples of physiological tubular instabilities which have predominantly been treated as purely growth induced, with little attention given to elasto-capillary effects. Exceptionally, consideration is given to the surface tension induced buckling of liquid lined tubes as a model for airway closure in [14], and insights into elasto-capillary circumferential buckling instabilities in tubes under axial loading [15], growth [16] and uniform pressure and geometric eversion [17] have very recently transpired.

The well known peristaltic instability in which soft slender cylinders adopt axisymmetric, localised beads under bulk and surface stresses has drawn much attention in recent years [18–23]. This bifurcation phenomenon can occur in stretched nerve fibres [24], in axons under mechanical trauma [25,26], and it has also been implicated in neurodegenerative disorders such as Alzheimer's and Parkinson's diseases [27]. Theoretically, it has been evidenced in [28] and [29] that the beading instability culminates in a "two-phase" state consisting of two regions of uniform but distinct axial stretch. Moreover, it was determined in [30] that a localised bulging or necking solution will initially occur depending on the loading path.

The beading instability is observable in hollow tubes which are filled with magnetic fluids [31], submerged in hydrophilic polymer solutions [32] and under growth [33], and has also been implicated in the synthesis of soft matter nanotubes [34] which have a variety of physical, biological and chemical applications [35]. Most interestingly, interconnecting tubes termed *tunnelling nanotubes* have been observed between migrating cells, and allow for inter-cellular communications and migration support [36–41]. These nanotubes contain cytoskeletal filaments and microtubules internally and come under axial tension when the cells move apart. As is shown in Fig. 1, the formation of static localised beads has in-fact been observed in these nanotubes [42].

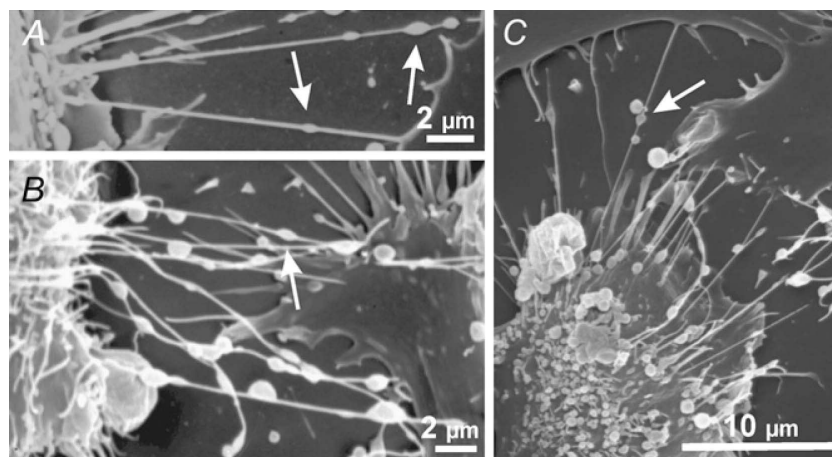


Figure 1: Tunnelling nanotubes (TNT's) have been observed between cells which migrate from one another, and are subject to axial stretching as the cells move further apart. Such tubes have been found to develop static localised axisymmetric beads. The images demonstrate this phenomena, showing beaded TNT's between human urothelial cells via scanning electron microscopy [42].

In spite of this, only very recently have the first steps been taken towards obtaining a concrete theoretical understanding of beading in hollow tubes. Finite Element Method simulations were

conducted for multiple fixed displacement boundary conditions in [43], whilst an infinite-wavelength instability in a cylindrical cavity under surface tension was found to be preferred in [22]. A linear bifurcation analysis of tubes under surface tension and axial stretching was initially conducted by [44], with further insights provided by [45]. In the latter, conditions for localised bifurcation are determined for three distinct boundary conditions. In Case 1, both lateral boundaries are traction-free and under surface tension, whilst in Case 2 (resp. Case 3), the inner (resp. outer) lateral surface is in smooth contact with a rigid boundary to prevent radial displacement and surface tension (with the other surface remaining traction-free and under surface tension). In Case 1, we originally thought in [45] that localised bifurcation was universally associated with negative surface tension, which is physically implausible. However, we have now discovered that localised solutions can in-fact exist in Case 1, and an explanation of this change in viewpoint is given shortly. However, we also showed in [15] that circumferential wrinkling modes can occur in Case 1 at a much lower surface tension than is predicted for localisation here, and so the latter is only a theoretical possibility. In Cases 2 and 3, the linear bifurcation analysis in [45] showed that localisation is possible and largely favourable over periodic axisymmetric modes. To provide further understanding of the beading instability in hollow tubes, we extend this work here by conducting a weakly non-linear near-critical analysis for Cases 2 and 3. We show absolutely that a localised solution can exist, and that the explicit nature of the possible bifurcations is highly dependant on the value of the principal axial stretch λ and the loading path. Given that Cases 1 and 2 have largely similar mathematical structures, we may postulate that the results and interpretations presented for Case 2 will also pertain to Case 1 in theory. By drawing upon previous FEM simulations [30,45] and recent experimental results for the analogous problem of localised bulging in tubes under axial stretching and internal inflation [46], we also give a complete interpretation of the post-bifurcation behaviour for multiple loading paths, and we hope that this will guide experimentalists in future studies.

The remainder of this paper is organised as follows. After formulating the problem in the next section, we extend in section 3 the derivation of the primary deformation and localised bifurcation conditions as presented originally in [45] to a general material model. We also explain why, contrary to our original claims, localised bifurcation is *theoretically* possible in Case 1. We then conduct a thorough weakly non-linear analysis in section 4 for Case 2 to decipher whether a localised solution can actually bifurcate from the primary state, and also to determine the explicit nature of possible bifurcations. In section 5, we provide for several loading paths a complete interpretation of the bifurcated solutions found in the previous section in order to guide future experimental works. Then, in section 6, we comment on the distinctions in the corresponding analysis for Case 3, focussing primarily on the regime of large thickness. Finally, concluding remarks are given in section 7.

2. Problem formulation

Consider a hyperelastic cylindrical tube with an initial inner radius A , outer radius B and axial half-length $L \gg B$. Under the general axisymmetric deformation

$$r = r(R, Z), \quad \theta = \Theta, \quad z = z(R, Z), \quad (2.1)$$

the inner and outer radii become a and b , respectively, whilst the axial half-length becomes $l \gg b$. A representative material particle in the undeformed and deformed configurations has the cylindrical polar coordinates $\mathbf{X} = (R, \Theta, Z)$ and $\mathbf{x} = (r, \theta, z)$, respectively. The corresponding deformation gradient \mathbf{F} is then defined through $d\mathbf{x} = \mathbf{F} d\mathbf{X}$ and takes the form

$$\mathbf{F} = \frac{\partial r}{\partial R} \mathbf{e}_r \otimes \mathbf{E}_R + \frac{\partial r}{\partial Z} \mathbf{e}_r \otimes \mathbf{E}_Z + \frac{r}{R} \mathbf{e}_\theta \otimes \mathbf{E}_\Theta + \frac{\partial z}{\partial R} \mathbf{e}_z \otimes \mathbf{E}_R + \frac{\partial z}{\partial Z} \mathbf{e}_z \otimes \mathbf{E}_Z, \quad (2.2)$$

where $(\mathbf{E}_R, \mathbf{E}_\Theta, \mathbf{E}_Z)$ and $(\mathbf{e}_r, \mathbf{e}_\theta, \mathbf{e}_z)$ are the orthonormal bases associated with the previously defined sets of coordinates. Assuming that the tube material is incompressible, we enforce the

following constraint of isochorism

$$\det \mathbf{F} = 1. \quad (2.3)$$

A strain-energy function w , which governs the constitutive behaviour of the tube, can then be introduced. For the sake of simplicity, we only consider strain-energy functions of the form

$$w = w(I_B), \quad (2.4)$$

where I_B is the first principal invariant of the left Cauchy–Green strain tensor $\mathbf{B} = \mathbf{F}\mathbf{F}^\top$, i.e. $I_B = \text{tr } \mathbf{B}$, with the superscript \top denoting transposition. This class of strain-energy functions has been shown to be suitable for many different materials under tension [47]. Two of the most common strain-energy functions of this form are the neo-Hookean and Gent material models, which take the respective forms

$$w = \frac{1}{2} \mu (I_B - 3), \quad \text{and} \quad w = -\frac{1}{2} \mu J_m \ln \left(1 - \frac{I_B - 3}{J_m} \right), \quad (2.5)$$

where J_m is the material extensibility constant. We note that, in the limit $J_m \rightarrow \infty$, the neo-Hookean material model is recovered from (2.5)₂. For the remainder of this paper we scale all lengths by B , all stresses by μ and the surface tension γ by μB . Therefore, we may set without loss of generality $B = 1$ and $\mu = 1$.

(a) Stream-function formulation

The problem can be elegantly re-formulated in terms of a single mixed co-ordinate stream function $\phi = \phi(R, z)$ such that the incompressibility constraint (2.3) is satisfied exactly [48]. This stream function is defined through the relations

$$r^2 = 2\phi_{,z}, \quad Z = \frac{1}{R} \phi_{,R}, \quad (2.6)$$

where a comma denotes partial differentiation with respect to the implied coordinate. Accordingly, \mathbf{F} can be re-expressed as such

$$\begin{aligned} \mathbf{F} = & \frac{1}{\sqrt{2\phi_{,z}}} \left[\phi_{,Rz} - R \frac{\phi_{,zz}}{\phi_{,Rz}} \frac{\partial}{\partial R} \left(\frac{1}{R} \phi_{,R} \right) \right] \mathbf{e}_r \otimes \mathbf{E}_R + \frac{R \phi_{,zz}}{\sqrt{2\phi_{,z}} \phi_{,Rz}} \mathbf{e}_r \otimes \mathbf{E}_z + \frac{\sqrt{2\phi_{,z}}}{R} \mathbf{e}_\theta \otimes \mathbf{E}_\theta \\ & - \frac{R}{\phi_{,Rz}} \frac{\partial}{\partial R} \left(\frac{1}{R} \phi_{,R} \right) \mathbf{e}_z \otimes \mathbf{E}_R + \frac{R}{\phi_{,Rz}} \mathbf{e}_z \otimes \mathbf{E}_z, \end{aligned} \quad (2.7)$$

and it then follows that I_B takes the form

$$I_B = \frac{1}{2\phi_{,z}} \left[\phi_{,Rz} - \frac{R \phi_{,zz}}{\phi_{,Rz}} \frac{\partial}{\partial R} \left(\frac{1}{R} \phi_{,R} \right) \right]^2 + \frac{1}{2} \frac{R^2 \phi_{,zz}^2}{\phi_{,z} \phi_{,Rz}^2} + \frac{2\phi_{,z}}{R^2} + \frac{R^2}{\phi_{,Rz}} - \frac{R^2}{\phi_{,Rz}^2} \left[\frac{\partial}{\partial R} \left(\frac{1}{R} \phi_{,R} \right) \right]^2. \quad (2.8)$$

Assuming initially a general case where both lateral boundaries are under surface tension, the total energy \mathcal{E} of the static axisymmetric solution is the sum of the bulk elastic energy and the surface energies on said boundaries

$$\mathcal{E} = 2\pi \int_{-\ell}^{\ell} \int_A^B \mathcal{L}_b dR dz + 2\pi \int_{-\ell}^{\ell} \left(\mathcal{L}_s^A + \mathcal{L}_s^B \right) dz, \quad (2.9)$$

where the bulk Lagrangian \mathcal{L}_b and surface Lagrangian's $\mathcal{L}_s^{A,B}$ are defined through

$$\mathcal{L}_b = \phi_{,Rz} w(I_B), \quad \mathcal{L}_s^{A,B} = \gamma \sqrt{2\phi_{,z} + \phi_{,zz}^2} \Big|_{R=A,B}. \quad (2.10)$$

Equilibrium of bulk elastic forces requires we satisfy Euler-Lagrange equation given by

$$\left(\frac{\partial \mathcal{L}_b}{\partial \phi_{,\beta\Gamma}} \right)_{,\beta\Gamma} - \left(\frac{\partial \mathcal{L}_b}{\partial \phi_{,\delta}} \right)_{,\delta} = 0. \quad (2.11)$$

The standard summation convention is applied here, with $\delta = R$ or z and $\beta\Gamma = RR, Rz$ or zz . Traction-free boundary conditions on the inner and outer lateral surfaces take the respective forms

$$\frac{\partial \mathcal{L}_b}{\partial \phi_{,R}} - \left(\frac{\partial \mathcal{L}_b}{\partial \phi_{,RR}} \right)_{,R} - \left(\frac{\partial \mathcal{L}_b}{\partial \phi_{,Rz}} \right)_{,z} - \left(\frac{\partial \mathcal{L}_s^A}{\partial \phi_{,zz}} \right)_{,zz} + \left(\frac{\partial \mathcal{L}_s^A}{\partial \phi_{,z}} \right)_{,z} = 0, \quad R = A, \quad (2.12)$$

$$\frac{\partial \mathcal{L}_b}{\partial \phi_{,R}} - \left(\frac{\partial \mathcal{L}_b}{\partial \phi_{,RR}} \right)_{,R} - \left(\frac{\partial \mathcal{L}_b}{\partial \phi_{,Rz}} \right)_{,z} + \left(\frac{\partial \mathcal{L}_s^B}{\partial \phi_{,zz}} \right)_{,zz} - \left(\frac{\partial \mathcal{L}_s^B}{\partial \phi_{,z}} \right)_{,z} = 0, \quad R = B, \quad (2.13)$$

where the change in sign of the surface energy terms is due to the opposing mean curvatures of the inner and outer boundaries. Where a lateral surface is in smooth contact with a rigid boundary (i.e. Cases 2 and 3 detailed previously), the traction-free condition on said surface is replaced by the requirement that the incremental radial displacement vanishes. This condition will be elucidated at a later stage in this paper. For any imposed displacement constraint, we have zero shear forces on both lateral surfaces, invoking a further two boundary conditions which are expressed as follows

$$\frac{\partial \mathcal{L}_b}{\partial \phi_{,RR}} = 0, \quad R = A, B. \quad (2.14)$$

3. Primary deformation and bifurcation conditions for localisation

We now narrow our focus towards the following primary axi-symmetric deformation, a sub-class of (2.1), which is theoretically possible for all strain-energy functions

$$r = r(R), \quad \theta = \Theta, \quad z = \lambda Z, \quad (3.1)$$

with λ defined as the principal axial stretch. The deformation gradient corresponding to (3.1) is

$$\mathbf{F} = \frac{\partial r}{\partial R} \mathbf{e}_r \otimes \mathbf{E}_R + \frac{r}{R} \mathbf{e}_\theta \otimes \mathbf{E}_\Theta + \lambda \mathbf{e}_z \otimes \mathbf{E}_Z. \quad (3.2)$$

We consider Cases 1, 2 and 3 separately for the remainder of this section.

(a) Case 1 - Traction-free lateral boundaries under surface tension

In Case 1, upon substitution of (3.2) into (2.3), the primary radial displacement r_0 which satisfies incompressibility exactly is found to take the form

$$r_0 = \sqrt{\lambda^{-1} (R^2 - A^2) + a^2}, \quad (3.3)$$

with the outer deformed radius b then becoming $r_0(B)$ and with a being an unknown parameter. Through integration of (2.6), the primary solution for ϕ , denoted ϕ_0 , and the associated expression for I_B are given by

$$\phi_0 = \frac{R^2 z}{2\lambda} + \frac{1}{2} \left(a^2 - \frac{A^2}{\lambda} \right) z, \quad I_0(R) = I_B|_{\phi=\phi_0} = \frac{(A^2 - a^2 \lambda)^2}{r_0^2 R^2 \lambda^2} + \frac{2 + \lambda^3}{\lambda}. \quad (3.4)$$

The tube is under the combined action of surface tension γ on $R = A, B$ and a resultant axial force \mathcal{N} , such that the total energy of the primary state is

$$\mathcal{E} = 2\pi \left[\int_{-\lambda L}^{\lambda L} \int_A^B \mathcal{L}_b dR dz + \int_{-\lambda L}^{\lambda L} (\mathcal{L}_s^A + \mathcal{L}_s^B) dz \right] - (\lambda - 1)\mathcal{N}, \quad \text{where } \phi = \phi_0. \quad (3.5)$$

On evaluating (3.5), we find the parameters λ and a determine the primary deformation completely, and equilibrium therefore requires that we satisfy $\partial\mathcal{E}/\partial\lambda = 0$ and $\partial\mathcal{E}/\partial a = 0$. From the former and latter, the following expressions for $\mathcal{N} = \mathcal{N}(\lambda, a)$ and $\gamma = \gamma(\lambda, a)$ are respectively obtained

$$\mathcal{N} = \pi \left[\frac{\gamma}{b}(a+b)^2 + 2 \int_A^B w_d I_{0\lambda} R dR \right], \quad \gamma = -\frac{b}{\lambda(a+b)} \int_A^B w_d I_{0a} R dR, \quad (3.6)$$

where $w_d = w'(I_0)$, $w_{dd} = w''(I_0)$ etc., $I_{0\lambda} = \partial I_0 / \partial \lambda$ and $I_{0a} = \partial I_0 / \partial a$. We note that the γ in (3.6)₁ is eliminated through substitution of (3.6)₂. For any loading scenario (e.g. fixed surface tension with monotonically varying axial stretch, or fixed axial stretch with increasing surface tension), the condition for localised bifurcation was determined in [45] to be

$$\mathcal{J}(\lambda, a) \equiv \frac{\partial \mathcal{N}}{\partial a} \frac{\partial \gamma}{\partial \lambda} - \frac{\partial \mathcal{N}}{\partial \lambda} \frac{\partial \gamma}{\partial a} = 0. \quad (3.7)$$

Now, it was originally thought that all values of λ and a which satisfy (3.7) are associated with negative values of $\gamma = \gamma(\lambda, a)$. Then, given that negative surface tension is physically implausible, it was concluded that localisation is not possible in this case. However, on re-examination of the contours $\mathcal{J}(\lambda, a) = 0$ in the (λ, a) plane, we find that there is in-fact an inconspicuous lower branch present in the regime of extremely small a in addition to the main branch that we originally identified. It transpires that the values of λ and a along this branch correspond to *positive* values of γ (see Fig. 2), and so contrary to our initial thoughts, localisation is theoretically possible in Case 1. However, it was shown in [15] that the tube will bifurcate into an elliptic circumferential buckling mode at a far lower value of γ than for localisation, suggesting that the latter won't actually materialise in reality. As an example, for the neo-Hookean strain-energy with $A = 0.4$ and $\lambda = 1.7$ fixed, the critical surface tension at which bifurcation into a circumferential elliptic mode occurs is $\gamma_{\text{cr}} \approx 0.056$ [15], whereas for localisation the corresponding value is $\gamma_{\text{cr}} \approx 6.65$. Thus, in the rest of this paper our attention will be focused on the other two cases.

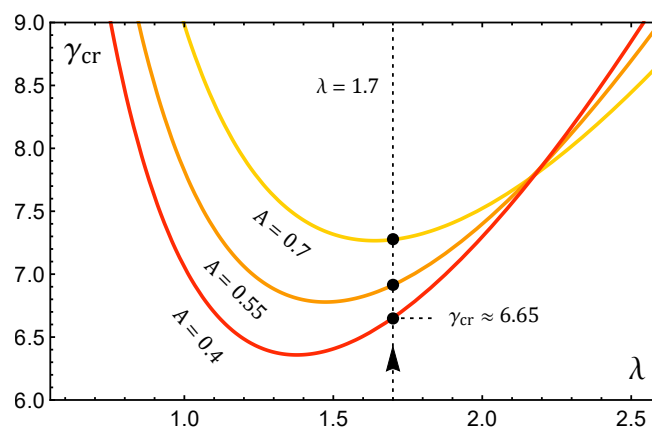


Figure 2: (Colour online) The variation of the critical surface tension γ_{cr} against λ for the neo-Hookean model with $A = 0.4, 0.55$ and 0.7 . We observe that each bifurcation curve has a minimum, and this was also shown to occur in [45] for Cases 2 and 3.

(b) Case 2 - Radially fixed inner lateral boundary free of surface tension

In Case 2, the restrictions imposed on the inner lateral surface require that the deformed inner radius is unchanged from its referential value. That is, we must enforce the constraint $a = A$. The total energy of the primary state is then the same as (3.5), except we must set $\mathcal{L}_s^A = 0$ since there is no surface tension on the inner lateral boundary here. Since a is known in Case 2, the single parameter λ is sufficient to determine the deformation completely, and equilibrium in the deformed configuration requires only that $\partial\mathcal{E}/\partial\lambda = 0$. Say we fix the surface tension γ and monotonically vary λ from some initial value, then this equilibrium equation yields an expression $\mathcal{N} = \mathcal{N}(\lambda)$ which is simply (3.6)₁ with $a \rightarrow A$ and γ equal to the chosen fixed value. Alternatively, we may fix \mathcal{N} and solve $\partial\mathcal{E}/\partial\lambda = 0$ for $\gamma = \gamma(\lambda)$ instead. The condition for localised bifurcation then reduces from (3.7) to $d\mathcal{N}/d\lambda = 0$ or $d\gamma/d\lambda = 0$, respectively. In the former case, the following implicit relationship between the critical axial stretch λ_{cr} for localisation and the fixed surface tension γ is obtained

$$\gamma = \frac{4b^3\lambda^3}{(A^2 - 1)^2} \int_A^B \frac{\partial}{\partial\lambda} (w_d I_{0\lambda}) R dR \Big|_{\lambda=\lambda_{\text{cr}}} . \quad (3.8)$$

An important feature of (3.8), and indeed (3.7) in Case 1, is that the associated bifurcation curves in the $(\lambda_{\text{cr}}, \gamma)$ plane have a minimum at $(\lambda_{\text{min}}, \gamma_{\text{min}})$, say; see Fig. 3. For each fixed $\gamma > \gamma_{\text{min}}$, there exists a single bifurcation value for λ either side of $\lambda = \lambda_{\text{min}}$, say $\lambda_{\text{cr}}^L < \lambda_{\text{min}}$ and $\lambda_{\text{cr}}^R > \lambda_{\text{min}}$, which corresponds to the maximum and minimum of $\mathcal{N} = \mathcal{N}(\lambda)$, respectively. In the limit $\gamma \rightarrow \gamma_{\text{min}}$, these two extrema of \mathcal{N} coalesce to form an inflection point, and for any $\gamma < \gamma_{\text{min}}$, \mathcal{N} is a monotonically increasing function of λ and localised bifurcation cannot occur.

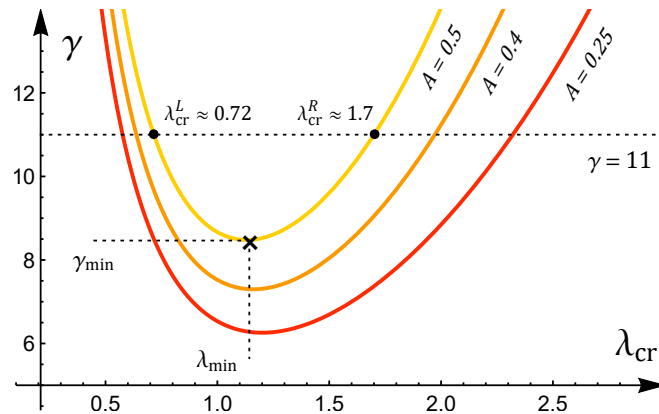


Figure 3: (Colour online) The bifurcation condition (3.8) plotted in the $(\lambda_{\text{cr}}, \gamma)$ plane for the Gent material model (2.5)₂. The material extensibility is fixed at $J_m = 100$, and the tube thickness's considered are $A = 0.25$ (red), $A = 0.4$ (orange) and $A = 0.5$ (yellow). Each bifurcation curve has a minimum at $(\lambda_{\text{cr}}, \gamma) = (\lambda_{\text{min}}, \gamma_{\text{min}})$. For instance, for $A = 0.5$ we have $(\lambda_{\text{min}}, \gamma_{\text{min}}) \approx (1.13, 8.48)$ as marked by the black cross. Then, for each fixed $\gamma > \gamma_{\text{min}}$, there exists a bifurcation point either side of $\lambda = \lambda_{\text{min}}$. For example, where $\gamma = 11$ and $A = 0.5$, the tube can bifurcate into a localised solution at $\lambda_{\text{cr}}^L \approx 0.72 < \lambda_{\text{min}}$ and $\lambda_{\text{cr}}^R \approx 1.7 > \lambda_{\text{min}}$ as shown by the black dots.

Now, for any strain-energy function of the form (2.4), \mathcal{N} is a monotonic function of λ up to the first bifurcation point encountered, which means that we can equivalently take \mathcal{N} or λ as the control parameter in this scenario. A special significance of this fact can be explained as follows. When fixing $\gamma > \gamma_{\text{min}}$ with zero axial force \mathcal{N} initially, an axial stretch $\lambda < \lambda_{\text{cr}}^L$ is produced. Indeed, this initial axial stretch can be related implicitly to γ by setting $\mathcal{N} = \mathcal{N}(\lambda)$ to zero; see Fig. 4 (b). Now, we have established that the bifurcation value $\lambda_{\text{cr}}^L < \lambda_{\text{min}}$ (resp. $\lambda_{\text{cr}}^R > \lambda_{\text{min}}$) corresponds

to the maximum (resp. minimum) of \mathcal{N} with respect to λ . As we increase λ from its starting value, we transverse along the $\mathcal{N} - \lambda$ curve from left to right. As such, we will always encounter the maximum first since $\mathcal{N} = \mathcal{N}(\lambda)$ is monotonically increasing up to this point. Thus, it is only the bifurcated solution corresponding to this maximum that is of interest in this scenario. Alternatively, we could apply a dead load to an end of the tube such that an initial axial stretch $\lambda > \lambda_{\text{cr}}^R$ is produced. We could then theoretically decrease the axial load until the tube bifurcates into the solution corresponding to the minimum of \mathcal{N} . It is noted however that this approach lacks physical viability since it is somewhat unrealistic to expect soft slender tubes to withstand such a dead load. The previously detailed thought experiment is illustrated in Fig. 4 (a) for a representative case.

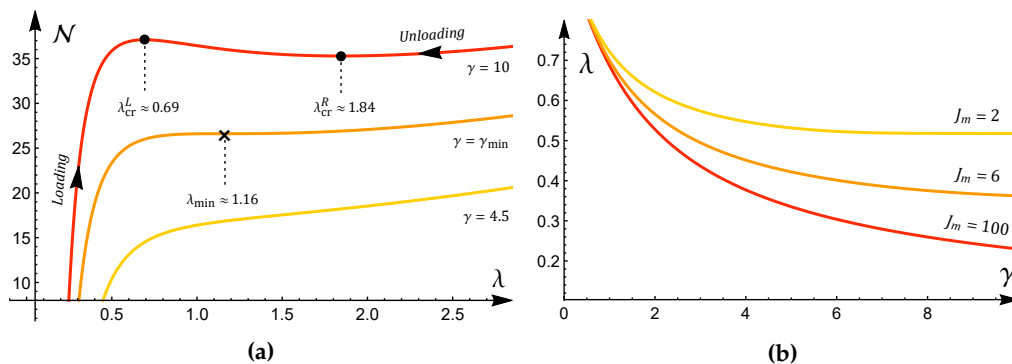


Figure 4: (Colour online) (a) The variation of the resultant axial force \mathcal{N} with respect to λ for the Gent material model (2.5)₂ with $J_m = 100$ and $A = 0.4$. The orange curve corresponding to $\gamma = \gamma_{\text{min}} \approx 7.299$ has an inflection point at $\lambda = \lambda_{\text{min}} \approx 1.16$. At $\gamma = 10 > \gamma_{\text{min}}$ (red curve), $\mathcal{N} = \mathcal{N}(\lambda)$ is non-monotonic and has a maximum (resp. minimum) at $\lambda_{\text{cr}}^L \approx 0.69 < \lambda_{\text{min}}$ (resp. $\lambda_{\text{cr}}^R \approx 1.84 > \lambda_{\text{min}}$). Say we fix $\gamma = 10$ with $\mathcal{N} = 0$ initially, then as λ is increased from its corresponding initial value, we transverse along the red curve in the direction of the *loading* arrow and we inevitably reach $\lambda = \lambda_{\text{cr}}^L$ first. If $\mathcal{N} > 0$ is fixed such that $\lambda > \lambda_{\text{cr}}^R$ initially, we instead transverse in the direction of the *unloading* arrow, and reach $\lambda = \lambda_{\text{cr}}^R$ first. (b) A plot of the starting values of λ against fixed γ when \mathcal{N} is initially zero for $A = 0.4$ and three distinct values of J_m .

(i) A spectral interpretation

The analysis presented previously can be captured and extended by a spectral eigensystem approach. On taking λ as the control parameter with γ fixed, we enforce the ansatz $\phi = \phi_0 + \varepsilon f(R) e^{\alpha z}$, where $\varepsilon \ll 1$ and α is the spectral parameter to be determined. On substituting said solution into (2.11) and the associated boundary conditions, we obtain at $O(\varepsilon)$ a linear eigenvalue problem in terms of f which can be expressed as the following system of matrix equations

$$\frac{d\mathbf{f}}{dR} = \mathbf{A}(R, \alpha)\mathbf{f}, \quad \mathbf{B}_1(A, \alpha)\mathbf{f} = \mathbf{0}, \quad \mathbf{B}_2(B, \alpha)\mathbf{f} = \mathbf{0}, \quad (3.9)$$

where $\mathbf{f} = [f, f', f'', f''']^\top$ and the matrices \mathbf{A} , \mathbf{B}_1 and \mathbf{B}_2 can be obtained from the supplementary *Mathematica* [49] files by making the substitution $k \rightarrow -i\alpha$. The eigensystem (3.9) can be solved numerically through a determinant shooting method, and we refer the reader to [45] for details of its implementation. It is found that, on fixing γ , the system (3.9) has a trivial eigenvalue $\alpha = 0$, infinitely many complex eigenvalues and infinitely many real eigenvalues $\alpha = \pm\alpha_1, \pm\alpha_2, \pm\alpha_3 \dots$, where $|\alpha_1| < |\alpha_2| < |\alpha_3| < \dots$. In Fig. 5, we study the change in α_1^2 for a representative case as we monotonically vary the load parameter λ .

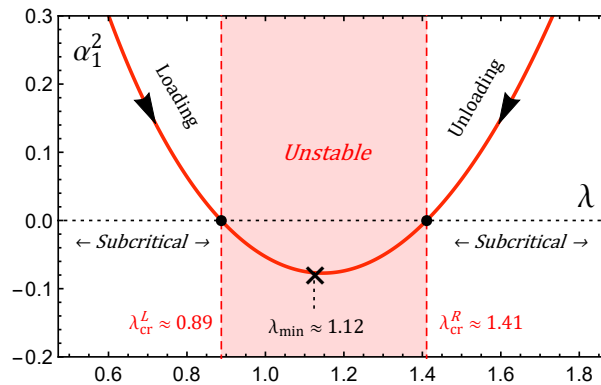


Figure 5: The variation of α_1^2 with respect to λ for $A = 0.5$ and $\gamma = 10$.

Say that, on fixing $\gamma > \gamma_{\min}$, we take $\mathcal{N} = 0$, producing an initial axial stretch $\lambda < \lambda_{\text{cr}}^L$. As λ is increased from this value, we transcend along the red curve in Fig. 5 in the direction of the arrow marked *loading*. We observe that α_1^2 is positive, and hence $\pm\alpha_1$ are non zero and real, up to the point $\lambda = \lambda_{\text{cr}}^L$ (as indicated by the left-most black dot), where $\alpha_1^2 = 0$. Therefore, bifurcation into a localised solution coincides with zero becoming a triple eigenvalue of the system (3.9), and axial stretches below this bifurcation value lie in the sub-critical regime wherein ϕ admits exponential behaviour. Beyond this bifurcation value, we enter the unstable regime, and we see that α_1^2 becomes negative, with $\pm\alpha_1$ therefore becoming purely imaginary. Thus, it is only *after* localised bifurcation occurs that the eigensystem (3.9) can support periodic solutions, and this was also shown to be the case in [45] for fixed $\lambda > 1$ and varying γ . Notwithstanding, if \mathcal{N} is fixed such that $\lambda > \lambda_{\text{cr}}^R$ initially and we unload from this point, the previous interpretations are also still valid. However, we transcend along the curve in Fig. 5 in the direction of the *unloading* arrow, and localisation occurs at the right-most black dot instead.

(c) Case 3 - Radially fixed outer lateral boundary free of surface tension

In Case 3, since the radial displacement of the *outer* lateral surface is now prohibited, the constraint $b = B$ is instead enforced, and we may then determine that the inner deformed radius $a = \sqrt{\lambda^{-1}(A^2 - 1) + 1}$. To ensure that this expression for a is real, we require that $\lambda > 1 - A^2$, and in the limit $a \rightarrow 0$, the axial stretch $\lambda \rightarrow 1 - A^2$. We note however that, in this limit, the traction-free assumption is violated since the inner surface comes into self-contact. The total energy of the primary solution is again slightly modified from (3.5) since \mathcal{L}_s^B must be zero. Then, for fixed γ , the resultant axial force \mathcal{N} can be obtained from the equilibrium equation $\partial\mathcal{E}/\partial\lambda = 0$, and is found to be equivalent to (3.6)₁ but with the expressions for a and b in Case 3 substituted. The corresponding localised bifurcation condition is again $d\mathcal{N}/d\lambda = 0$, from which we obtain

$$\gamma = \frac{4a^3\lambda^3}{(A^2 - 1)^2} \int_A^B \frac{\partial}{\partial\lambda} (w_d I_{0\lambda}) R dR \Big|_{\lambda=\lambda_{\text{cr}}}. \quad (3.10)$$

If the resultant axial force is zero when applying the fixed surface tension, an axial stretch $1 - A^2 < \lambda < 1$ is produced (see Fig. 6), and a contraction of the tube's inner surface occurs. Indeed, the level of contraction is an increasing function of γ .

Since localisation in Case 1 is generally preceded by circumferential buckling modes, the weakly non-linear analysis in the following section is tailored towards Case 2 with the view that determined results will also apply to Case 1 in theory due to a similarity in mathematical structure. However, an overview of the results for Case 3 (and their distinctions from Cases 1 and 2) is given in section 6 for completeness. In the next section, we not only validate (3.7), but we also demonstrate that the bifurcation solutions corresponding to the maximum and minimum of

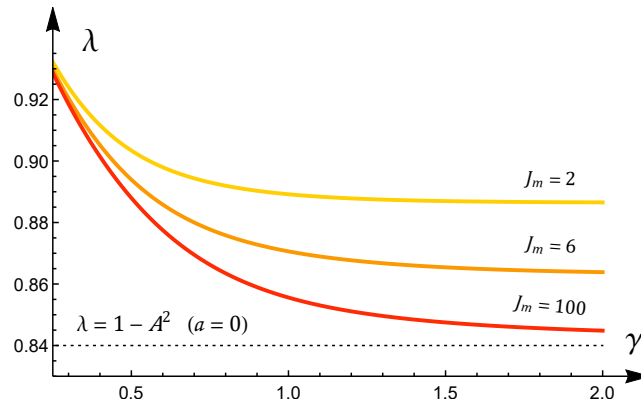


Figure 6: (Colour online) The variation of the starting value of λ with respect to γ when \mathcal{N} is initially zero for $A = 0.4$ and three distinct values of J_m . The dotted horizontal asymptote is situated at $\lambda = 1 - A^2$ where the inner deformed radius $a = 0$. For each fixed γ , we observe that the contraction of the inner surface is greater in tubes with greater extensibility limits.

\mathcal{N} are localised necking and bulging, respectively. We then investigate whether these solutions occur *super-critically* or *sub-critically*.

4. Weakly non-linear near-critical analysis

In a weakly non-linear analysis, we are interested in the relationship between the increment of the control parameter from its bifurcation value and the amplitude of the associated localised solution. Further insights into the principal ideas of such an analysis can be found in [50]. Here, we construct an exhaustive weakly non-linear analysis for Case 2 in terms of a general material model and focus on two main loading scenarios. Namely, we fix γ and take λ as the control parameter, or we fix λ and take γ as the control parameter.

(a) Taking λ as the control parameter with fixed γ .

In the previous section we outlined that \mathcal{N} or λ can equivalently be taken as the control parameter when γ is fixed, and we proceed with the latter of these choices here. We also showed that the bifurcation solution corresponding to a triple zero eigenvalue of (3.9) is preferred in this loading scenario. Thus, guided by the framework in [50], we consider a small deviation of the axial stretch from its critical value λ_{cr}

$$\lambda = \lambda_{\text{cr}} + \varepsilon \lambda_1, \quad (4.1)$$

where $\varepsilon \ll 1$ is a positive parameter and λ_1 is a constant of $O(1)$. As a consequence of the results illustrated in Fig 5, λ is locally parabolic with respect to the axial wavenumber $k = -i\alpha$ in this near-critical regime, motivating the introduction of a far distance variable s such that

$$s = \varepsilon^{1/2} z. \quad (4.2)$$

Extending (3.4), we look for a solution of the form

$$\phi = \phi_0 + \varepsilon^{1/2} \left\{ \phi_1^{(1)}(R, s) + \varepsilon \phi_1^{(2)}(R, s) + \varepsilon^2 \phi_1^{(3)}(R, s) + \dots \right\}. \quad (4.3)$$

Then, the corresponding expansions for the mixed co-ordinates given in (2.6) are as follows

$$r = r_{\text{cr}} + \frac{\varepsilon}{r_{\text{cr}}} \left\{ \frac{\lambda_1}{2\lambda_{\text{cr}}^2} (A^2 - R^2) + \phi_{1,s}^{(1)} \right\} + \dots, \quad Z = \frac{z}{\lambda_{\text{cr}}} + \frac{\varepsilon^{1/2}}{R} \phi_{1,R}^{(1)} - \varepsilon \frac{z\lambda_1}{\lambda_{\text{cr}}^2} + \dots, \quad (4.4)$$

where r_{cr} is simply r_0 as given by (3.3) evaluated at $\lambda = \lambda_{cr}$. On substituting (4.3) into (2.11) and the associated boundary conditions, we obtain a hierarchy of boundary value problems by equating the coefficients of like powers of ε . To leading order, we obtain the governing equation

$$\mathcal{L}[\phi_1^{(1)}] = 0, \quad (4.5)$$

and the associated boundary conditions

$$\mathcal{B}_1[\phi_1^{(1)}]_{R=1} = 0, \quad \mathcal{B}_2[\phi_1^{(1)}]_{R=1, A} = 0, \quad \phi_{1,s}^{(1)}(A, s) = 0. \quad (4.6)$$

We note that (4.6)_{1,2} are derived from (2.12) and (2.14), respectively, whilst (4.6)₃ ensures that the leading order incremental radial displacement vanishes on $R = A$; see (4.4)₁. The three differential operators \mathcal{L} , \mathcal{B}_1 and \mathcal{B}_2 are defined as such

$$\mathcal{L} = \frac{\partial}{\partial R} \frac{1}{R} \frac{\partial}{\partial R} R w_d \frac{\partial}{\partial R} \frac{1}{R} \frac{\partial}{\partial R}, \quad \mathcal{B}_1 = \frac{1}{R} \frac{\partial}{\partial R} R w_d \frac{\partial}{\partial R} \frac{1}{R} \frac{\partial}{\partial R}, \quad \mathcal{B}_2 = \frac{\partial}{\partial R} \frac{1}{R} \frac{\partial}{\partial R}, \quad (4.7)$$

and can be shown to satisfy the following identity

$$\int_A^1 \{g \mathcal{L}[f] - f \mathcal{L}[g]\} dR = \left[g \mathcal{B}_1[f] - f \mathcal{B}_1[g] + f' w_d \mathcal{B}_2[g] - g' w_d \mathcal{B}_2[f] \right]_A^1, \quad (4.8)$$

where f and g are sufficiently smooth functions of R with the property $f(A) = g(A) = 0$. Indeed, (4.8) is a consequence of the self-adjointness of \mathcal{L} , and will be applied later to derive the amplitude equation. Through repeated integration of (4.5), the following general solution for $\phi_1^{(1)}$ is determined

$$\phi_1^{(1)} = C_1(s)R^2 + C_2(s)\xi_2(R) + C_3(s)\xi_3(R) + C_4(s), \quad (4.9)$$

where

$$\xi_2(R) = \int_A^R u \int_A^u \frac{t}{w_d} dt du \quad \text{and} \quad \xi_3(R) = \int_A^R u \int_A^u \frac{1}{t w_d} dt du. \quad (4.10)$$

On substituting (4.9) into (4.6)₂, we find that C_2 and C_3 must necessarily be zero, whilst (4.6)₁ is automatically satisfied and (4.6)₃ requires that $C_4'(s) = -A^2 C_1'(s)$. We may integrate the latter expression with respect to s and set the additive constant to zero without loss of generality since the displacements (4.4) depend only on the partial derivatives of $\phi_1^{(1)}$. This statement also holds true at higher orders. Thus, the particular leading order solution is

$$\phi_1^{(1)} = C_1(s) (R^2 - A^2), \quad (4.11)$$

where $C_1(s)$ is to be determined. At the next order order, we have the following governing equation

$$\mathcal{L}[\phi_1^{(2)}] = p_1(R) C_1''(s), \quad \text{where} \quad p_1 = p_1^{(1)} w_d + p_1^{(2)} w_{dd} + p_1^{(3)} w_{ddd}, \quad (4.12)$$

with the functions $p_1^{(m)}$ ($m = 1, 2$ and 3) available in the supplementary Mathematica files. The associated traction-free and zero shear boundary conditions are then given respectively as follows

$$\mathcal{B}_1[\phi_1^{(2)}] = k_1 C_1''(s) = \left\{ \frac{(1-A^2)\gamma}{2b^3 \lambda_{cr}} + k_1^{(2)} w_d + k_1^{(3)} w_{dd} \right\} C_1''(s), \quad R = 1, \quad (4.13)$$

$$\mathcal{B}_2[\phi_1^{(2)}] = \frac{R(R^2 - A^2)}{r_{cr}^2 \lambda_{cr}^2} C_1''(s), \quad R = 1, A,$$

with the constants $k_1^{(m)}$ ($m = 2, 3$) likewise given in our Mathematica files. Furthermore, the boundary condition enforcing zero incremental radial displacement at $R = A$ at this order is

$\phi_{1,s}^{(2)}(A, s) = 0$. A general solution to (4.12) is

$$\phi_1^{(2)} = D_1(s) R^2 + D_2(s) \xi_2(s) + D_3(s) \xi_3(s) + D_4(s) + C_1''(s) \mathcal{P}(R), \quad (4.14)$$

where $\mathcal{P}(R)$ is a particular integral given by

$$\mathcal{P}(R) = \int_A^R x \int_A^x \frac{1}{v w_d} \int_A^v u \int_A^u p_1(t) dt du dv dx. \quad (4.15)$$

We note that $\mathcal{P}(R)$ is non-elementary, and so we evaluate it numerically using the procedure detailed in [46]. On substituting (4.14) into $\phi_{1,s}^{(2)}(A, s) = 0$ and (4.13)₂ at $R = A$, we find that D_3 and D_4 are linear in terms of D_1, D_2 and C_1'' . Then, on substituting (4.14) into (4.13)₁ and (4.13)₂ evaluated at $R = 1$, we obtain a matrix equation of the form $M \mathbf{d} = \mathbf{0}$, where $\mathbf{d} = [C_1''(s), D_2(s)]^\top$ and M is not written out for the sake of brevity. The existence of a non-trivial solution requires that $\det M = 0$, from which we obtain the bifurcation condition (3.8) and an expression for D_2 which is linear in C_1'' .

At the third order, the governing equation is

$$\mathcal{L} [\phi_1^{(3)}] = p_1(R) D_1''(s) + p_2(R) C_1''''(s) + p_3(R) C_1''(s) (\lambda_1 - 2 \lambda_{\text{cr}}^2 C_1'(s)). \quad (4.16)$$

The associated traction-free and zero shear boundary conditions also contain non-linear inhomogeneous terms. At $R = 1$, the former is expressed as follows

$$\mathcal{B}_1 [\phi_1^{(3)}] = k_1 D_1''(s) + k_2 C_1''''(s) + k_3 C_1''(s) (\lambda_1 - 2 \lambda_{\text{cr}}^2 C_1'(s)), \quad (4.17)$$

and at $R = 1$ and A the latter takes the form

$$\mathcal{B}_2 [\phi_1^{(3)}] = \frac{R(R^2 - A^2)}{r_{\text{cr}}^2 \lambda_{\text{cr}}^2} D_1''(s) + s_2(R) C_1''''(s) + s_3(R) C_1''(s) (\lambda_1 - 2 \lambda_{\text{cr}}^2 C_1'(s)). \quad (4.18)$$

The functions $p_{2,3}$, $s_{2,3}$ and the constants $k_{2,3}$ are lengthy and so we do not display them here. As is typical with this type of problem, there is no need to solve the above third order boundary value problem for $\phi_1^{(3)}$ in the conventional manner if we are only seeking the amplitude equation for $C_1(s)$. Since the homogeneous form of this third order boundary value problem has a non-trivial solution, it follows that the inhomogeneous terms on the right hand side of (4.16) - (4.18) must satisfy a solvability condition. Indeed, said condition comes in the form of the identity (4.8). By setting g equal to the first order solution (4.11) and $f = \phi_1^{(m)}$ ($m = 2, 3$), (4.8) reduces to

$$\int_A^1 (R^2 - A^2) \mathcal{L} [\phi_1^{(m)}] dR = \left[(R^2 - A^2) \mathcal{B}_1 [\phi_1^{(m)}] - 2 R w_d \mathcal{B}_2 [\phi_1^{(m)}] \right]_A^1. \quad (4.19)$$

We note that $\mathcal{L} [\phi_1^{(m)}]$, $\mathcal{B}_1 [\phi_1^{(m)}]$ and $\mathcal{B}_2 [\phi_1^{(m)}]$ are each equal to expressions which involve only lower order solutions. Thus, on setting $m = 2$ in (4.19), after evaluating the integral and making appropriate rearrangements, we recover the bifurcation condition (3.8). Then, where $m = 3$, we yield the desired amplitude equation. On integrating once and setting the arbitrary constant to zero for decay solutions, we obtain

$$\mathcal{A}'' = \lambda_1 \kappa_1 \mathcal{A} + \kappa_2 \mathcal{A}^2, \quad (4.20)$$

where the amplitude $\mathcal{A}(s) = C_1'(s)$ and the coefficients $\kappa_{1,2}$ are discussed below.

(i) Analysis of the amplitude equation

For any strain-energy function of the form (2.4), the special relationship $\kappa_2 = -\lambda_{\text{cr}}^2 \kappa_1$ holds and can be explained as follows. We note firstly that, to order ε , the principal axial stretch is

$$\lambda = \lambda_{\text{cr}} + \varepsilon \left(\lambda_1 - 2\lambda_{\text{cr}}^2 \mathcal{A}(s) \right). \quad (4.21)$$

When γ is fixed, the bifurcation points $\lambda = \lambda_{\text{cr}}$ occur at the extrema of the resultant axial force, and so $\mathcal{N} = \mathcal{N}(\lambda)$ is parabolic in a small neighbourhood of $\lambda = \lambda_{\text{cr}}$. Thus, provided the amplitude $\mathcal{A}(s)$ is constant, (4.1) and (4.21) are two possible near-critical solutions for λ which must be equidistant from $\lambda = \lambda_{\text{cr}}$ and yield the same value of \mathcal{N} . That is, we must have

$$\lambda_{\text{cr}} - \left\{ \lambda_{\text{cr}} + \varepsilon \left(\lambda_1 - 2\lambda_{\text{cr}}^2 \mathcal{A}(s) \right) \right\} = (\lambda_{\text{cr}} + \varepsilon \lambda_1) - \lambda_{\text{cr}}, \quad (4.22)$$

from which we obtain $\mathcal{A}(s) = \lambda_1 / \lambda_{\text{cr}}^2$. Then, on substituting this expression for \mathcal{A} back into (4.20), the relation $\kappa_2 = -\lambda_{\text{cr}}^2 \kappa_1$ follows.

Whilst the determined expression for κ_1 is analytical, it is largely in terms of integrals which cannot be evaluated explicitly. Thus, for the chosen material model, κ_1 is determined numerically by evaluating these integrals through the same approach as detailed in appendix B. On specifying the Gent strain-energy function with $J_m = 100$, we present in Tables 1 and 2 numerical values of κ_1 corresponding to $\lambda_{\text{cr}} = \lambda_{\text{cr}}^L$ and $\lambda_{\text{cr}} = \lambda_{\text{cr}}^R$, respectively. We observe that, in the former and latter cases, κ_1 is respectively negative and positive, suggesting that κ_1 is inexplicitly proportional to (and of the same sign as) $d\gamma/d\lambda|_{\lambda=\lambda_{\text{cr}}}$.

Table 1: Numerical values of κ_1 for the Gent material model with $J_m = 100$ and $\lambda_{\text{cr}} = \lambda_{\text{cr}}^L$.

	$\gamma = 10.5$	$\gamma = 11$	$\gamma = 11.5$	$\gamma = 12$	$\gamma = 12.5$	$\gamma = 13$
$A = 0.2$	-1.2349	-1.2548	-1.2703	-1.2823	-1.2913	-1.2977
$A = 0.3$	-1.2226	-1.2523	-1.2766	-1.2965	-1.3128	-1.3261
$A = 0.4$	-1.1642	-1.2108	-1.2497	-1.2825	-1.3103	-1.3341
$A = 0.5$	-0.9856	-1.0667	-1.1336	-1.1897	-1.2375	-1.2788
$A = 0.6$	-0.2857	-0.5763	-0.7545	-0.8698	-0.9685	-1.05002

In fact, we can offer a clear interpretation of this observation by extending the previously discussed spectral eigensystem approach to the near critical regime. We refer the reader to Fig. 7 which supplements the following remarks. Consider the linearised form of the amplitude equation (4.20). On assuming a solution of the form $\mathcal{A} = e^{\alpha s}$, the spectral parameter α is found to have two non-trivial values, namely $\pm\alpha_1 = \pm\sqrt{\lambda_1 \kappa_1}$. We note that these are the same $\pm\alpha_1$ from the previous section defined analytically in the near-critical regime. From Fig. 5, we expect that bounded periodic solutions are possible only in the super-critical regime, and so we anticipate

Table 2: Numerical values of κ_1 for the Gent material model with $J_m = 100$ and $\lambda_{\text{cr}} = \lambda_{\text{cr}}^R$.

	$\gamma = 10.5$	$\gamma = 11$	$\gamma = 11.5$	$\gamma = 12$	$\gamma = 12.5$	$\gamma = 13$
$A = 0.2$	1.3889	1.4339	1.4748	1.5124	1.5472	1.5796
$A = 0.3$	1.3158	1.3632	1.4045	1.4433	1.4777	1.5092
$A = 0.4$	1.1925	1.2483	1.2965	1.3387	1.37604	1.4094
$A = 0.5$	0.96797	1.0495	1.1167	1.1735	1.2221	1.2643
$A = 0.6$	0.2717	0.5545	0.7158	0.8326	0.9237	0.9979

that \mathcal{A} admits exponential behaviour in the sub-critical regime. Where \mathcal{N} is initially zero and then monotonically increased (as indicated by the arrow marked *loading* in Fig. 7 (a)), λ_1 is negative (resp. positive) in the sub-critical (resp. super-critical) regime and we therefore require that $\kappa_1 < 0$ for \mathcal{A} to take its expected form. Note also that, in the limit $\lambda_1 \rightarrow 0^-$, bifurcation into a localised solution at $\lambda = \lambda_{cr}^L$ occurs in tandem with zero becoming a triple eigenvalue; see Fig. 7 (b). In contrast, where \mathcal{N} is non-zero initially such that $\lambda > \lambda_{cr}^R$ and we unload the tube gradually, λ_1 is positive (resp. negative) in the sub-critical (resp. super-critical) regime, and we therefore require that $\kappa_1 > 0$ instead.

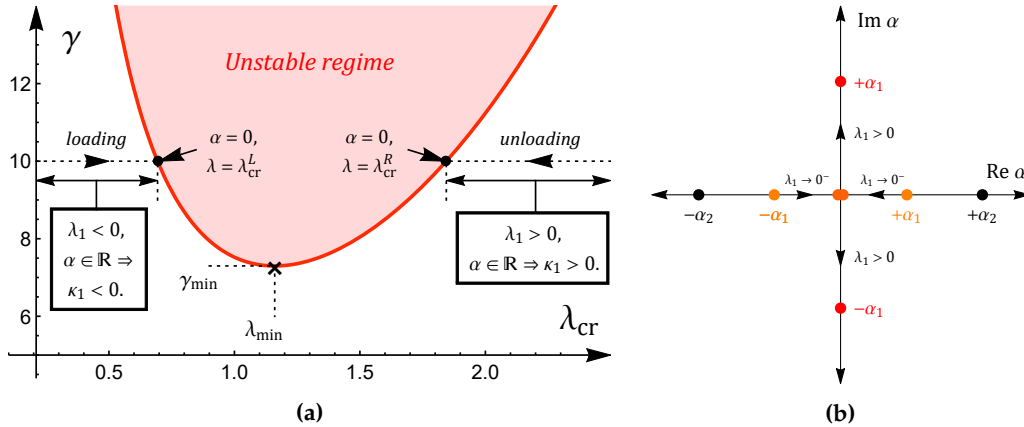


Figure 7: (a) Regimes of sub-criticality (white region) and instability (red region) in the (λ_{cr}, γ) plane and (b) positions of the eigenvalues $\pm\alpha_1 = \pm\sqrt{\lambda_1\kappa_1}$ in the complex plane as λ passes from the sub-critical to unstable regime. The red curve in (a) is the bifurcation condition (3.8) for the Gent material model with $A = 0.4$ and $J_m = 100$. Say we fix $\gamma = 10$, then we move in the direction of the *loading* or *unloading* arrow depending on the initial value of \mathcal{N} . In (b), we focus on the *loading* path, and in the sub-critical regime $\lambda_1 < 0$ the positions of $\pm\alpha_1$ are marked by the orange dots. As $\lambda_1 \rightarrow 0^-$, $\pm\alpha_1$ will translate along the $\text{Re } \alpha$ axis towards the origin where they coalesce at the point of bifurcation. In the unstable regime $\lambda_1 > 0$, the positions of $\pm\alpha_1$ are marked by the red dots. We observe that a movement away from the origin onto the positive and negative $\text{Im } \alpha$ axes occurs, at which point periodic solutions become possible.

A localised solution to the amplitude equation (4.20) is a standing solitary wave given by

$$\mathcal{A}(s) = -\frac{3\lambda_1\kappa_1}{2\kappa_2} \text{sech}^2\left(\frac{1}{2}\sqrt{\lambda_1\kappa_1}s\right), \quad (4.23)$$

with the radial displacement (4.4)₁ then becoming

$$r(R, z) = r_{cr} + \varepsilon \frac{(A^2 - R^2)}{2\lambda_{cr}^2 r_{cr}} \left(\lambda_1 - 2\lambda_{cr}^2 \mathcal{A}(\varepsilon^{1/2}z) \right) + \dots \quad (4.24)$$

Given the aforementioned behaviour of κ_1 , for (4.23) to be valid for $\lambda_{cr} = \lambda_{cr}^L$ (resp. $\lambda_{cr} = \lambda_{cr}^R$) we require that $\lambda_1 < 0$ (resp. $\lambda_1 > 0$). It then follows that the localised solution (4.23) is a dark soliton (necking) for $\lambda_{cr} = \lambda_{cr}^L$, whereas (4.23) corresponds to a bright soliton (bulging) for $\lambda_{cr} = \lambda_{cr}^R$. Both of these solutions occur sub-critically, with the former and latter arising from the *loading* and *unloading* scenarios alluded to in Fig. 7 (a). However, we reiterate that the *unloading* scenario is somewhat physically implausible in this context, and hence the localised necking solution garners the majority of practical interest here. In Fig. 8, we illustrate the radial displacement profile (4.24) for the *loading* and *unloading* scenarios.

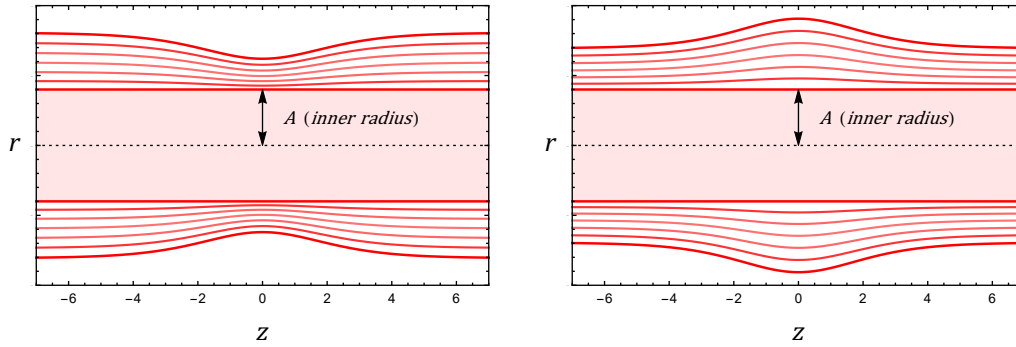


Figure 8: (Colour online) The displacement profile (4.24) in the *loading* (left) and *unloading* (right) scenario, where $\gamma = 11$, $A = 0.4$ and $J_m = 100$. The light red interior represents the rigid internal cylinder which prevents the radial displacement of the inner surface of the tube.

For the alternate loading scenario of fixed λ and varying γ (which is to be discussed later), the corresponding solitary wave solution in the case of a solid cylinder was shown to diverge in the limit $\lambda \rightarrow \lambda_{\min}$ [30]. In contrast, due to the special relationship between κ_1 and κ_2 here, our (4.23) remains finite in said limit. However, since $\kappa_1 \rightarrow 0$ as $\lambda \rightarrow \lambda_{\min}$, the form of (4.23) suggests that a rescaling of the far distance variable s is instead required. We analyse this limiting case separately in the next subsection.

(ii) The limit $\lambda_{\text{cr}} \rightarrow \lambda_{\min}$

We introduce the following re-scaled form of s

$$\hat{s} = \varepsilon^{1/2} s = \varepsilon z. \quad (4.25)$$

Since γ is locally parabolic with respect to λ_{cr} about $(\lambda_{\min}, \gamma_{\min})$, an $O(\varepsilon^2)$ deviation of γ from γ_{\min} is considered such that

$$\lambda = \lambda_{\min} + \varepsilon \hat{\lambda}_1, \quad \gamma = \gamma_{\min} + \varepsilon^2 \hat{\gamma}_1, \quad (4.26)$$

where $\hat{\lambda}_1$ and $\hat{\gamma}_1$ are constants of $O(1)$. Given (4.25), we implement the following re-scaling of ϕ

$$\phi = \phi_0 + \hat{C}_1(\hat{s}) \left(R^2 - A^2 \right) + \varepsilon \left\{ \hat{\phi}_1^{(1)} + \varepsilon \hat{\phi}_1^{(2)} + \varepsilon^2 \hat{\phi}_1^{(3)} + \varepsilon^3 \hat{\phi}_1^{(4)} + \dots \right\}, \quad (4.27)$$

noting that, although $\phi_0 \sim \hat{C}_1(\hat{s})(R^2 - A^2)$ in (4.27), the first correction to the primary deformation gradient is in fact of $O(\varepsilon)$.

We then follow the same procedure as presented previously for the non-limit case. At $O(\varepsilon)$, we find that $\hat{\phi}_1^{(1)}$ must necessarily be zero. At $O(\varepsilon^2)$, the bifurcation condition (3.8) evaluated at $(\lambda, \gamma) = (\lambda_{\min}, \gamma_{\min})$ is obtained. Then, at $O(\varepsilon^3)$, we recover the equation $d\gamma/d\lambda|_{\lambda_{\min}} = 0$ which is satisfied automatically. At $O(\varepsilon^4)$, by setting $g = \hat{C}_1(\hat{s})(R^2 - A^2)$ and $f = \hat{\phi}_1^{(4)}$ in (4.19), the following amplitude equation for $\hat{A}(\hat{s}) = \hat{C}_1'(\hat{s})$ is obtained

$$\hat{A}'' = \left(\hat{\gamma}_1 \hat{\kappa}_1 + \hat{\lambda}_1^2 \hat{\kappa}_2 \right) \hat{A} - 2 \hat{\lambda}_1 \lambda_{\min}^2 \hat{\kappa}_2 \hat{A}^2 + \frac{4}{3} \lambda_{\min}^4 \hat{\kappa}_2 \hat{A}^3. \quad (4.28)$$

The coefficient $\hat{\kappa}_1$ takes the general form

$$\hat{\kappa}_1 = \frac{(1 - A^2)^2}{\hat{\kappa}_0 b^3 \lambda} \Big|_{\lambda = \lambda_{\min}}, \quad (4.29)$$

where $\hat{\kappa}_0$ is in terms of non-elementary integrals and depends on the choice of material model. Numerical values for $\hat{\kappa}_0$ when the Gent material model is deployed are given in Table 3 below.

Table 3: Numerical values of $\hat{\kappa}_0$ for several values of A and J_m .

	$A = 0.3$	$A = 0.4$	$A = 0.5$	$A = 0.6$	$A = 0.7$	$A = 0.8$
$J_m = 100$	-5.011	-4.7802	-4.4473	-3.9832	-3.3527	-2.5139
$J_m = 20$	-5.1527	-4.90001	-4.5425	-4.0532	-3.3986	-2.5383
$J_m = 10$	-5.2556	-4.9884	-4.6139	-4.1064	-3.4337	-2.557
$J_m = 6$	-5.3374	-5.0593	-4.6717	-4.1498	-3.4624	-2.5723
$J_m = 3$	-5.4387	-5.1477	-4.7441	-4.2042	-3.4985	-2.5915

We observe that $\hat{\kappa}_0$ (and hence $\hat{\kappa}_1$) is generally negative, and this fact can be interpreted as follows. For fixed $\hat{\gamma}_1 > 0$, the maximum and minimum of the resultant axial force \mathcal{N} are near the point of coalescence. On Taylor expanding \mathcal{N} around $(\lambda_{\min}, \gamma_{\min})$ and then solving $d\mathcal{N}/d\lambda = 0$, the bifurcation points for λ in a small neighbourhood of λ_{\min} are found to take the form

$$\lambda_{\text{cr}}^{L,R} = \lambda_{\min} + \varepsilon \hat{\lambda}_1^{L,R}, \quad \text{where} \quad \hat{\lambda}_1^{L,R} = \mp \sqrt{-2\hat{\gamma}_1 \frac{\partial^2 \mathcal{N}}{\partial \lambda \partial \gamma} \left(\frac{\partial^3 \mathcal{N}}{\partial \lambda^3} \right)^{-1}}, \quad (4.30)$$

with the derivatives of \mathcal{N} evaluated at $(\lambda_{\min}, \gamma_{\min})$. Say we take $\mathcal{N} = 0$ initially and then increase the axial stretch monotonically, then the first bifurcation point encountered will be $\lambda = \lambda_{\min} + \varepsilon \hat{\lambda}_1^L$. Now, consider the linearised form of (4.28) and let $\hat{\lambda}_1 = \hat{\lambda}_1^L + \delta \hat{\lambda}_1$. On assuming a solution of the form $\hat{A} = e^{\hat{\alpha} \hat{s}}$, the spectral parameter $\hat{\alpha}$ takes the non-trivial values $\pm \hat{\alpha}_1 = \pm \sqrt{\hat{\gamma}_1 \hat{\kappa}_1 + \hat{\lambda}_1^2 \hat{\kappa}_2}$. From the results in section 3, localised bifurcation must necessarily occur in the limits $\delta \hat{\lambda}_1 \rightarrow 0$ and $\pm \hat{\alpha}_1 \rightarrow 0$, and this can only be achieved if

$$\hat{\kappa}_2 = -\frac{\hat{\gamma}_1 \hat{\kappa}_1}{(\hat{\lambda}_1^L)^2} = \frac{1}{2} \hat{\kappa}_1 \frac{\partial^3 \mathcal{N}}{\partial \lambda^3} \left(\frac{\partial^2 \mathcal{N}}{\partial \lambda \partial \gamma} \right)^{-1} \Bigg|_{(\lambda_{\min}, \gamma_{\min})}. \quad (4.31)$$

In the sub-critical regime we have that $\delta \hat{\lambda}_1 < 0$, and hence $\hat{\lambda}_1 < \hat{\lambda}_1^L < 0$. Thus, for $\pm \hat{\alpha}_1$ to be real here as expected, we deduce with the aid of (4.31) that $\hat{\kappa}_1$ must necessarily be negative. Similarly, we have that $\hat{\lambda}_1^L < \hat{\lambda}_1 < 0$ in the unstable regime, and $\hat{\kappa}_1$ must remain negative for \hat{A} to admit the anticipated super-critical periodic behaviour. An analogous interpretation can be made when *unloading* from an initial axial force $\mathcal{N} > 0$, and the requirement that $\hat{\kappa}_1$ be negative remains true. Given this, we deduce that $\hat{\kappa}_2$ must generally be negative on substituting (3.6)₁ into (4.31). Furthermore, we may substitute $\lambda_{\text{cr}} = \lambda_{\text{cr}}^{L,R}$ into the counterpart of (4.22) for the limiting case to produce two constant solutions $\hat{A} = (\hat{\lambda}_1 \pm \hat{\lambda}_1^L)/\lambda_{\min}^2$. On inserting these constant solutions back into (4.28), two equations in terms of $\hat{\kappa}_{1,2}$ are obtained. From the first, the relation (4.31) is recovered, whilst the second equation gives the relationship between the quadratic and cubic coefficients in (4.28).

Alternatively, (4.28) can be expressed as the following one degree-of-freedom Hamiltonian system

$$\hat{A}'' = -\frac{\partial \hat{V}}{\partial \hat{A}}, \quad \text{where} \quad \hat{V} = -\frac{1}{3} \lambda_{\min}^4 \hat{\kappa}_2 \hat{A}^2 (\hat{A} - \hat{A}_0^+) (\hat{A} - \hat{A}_0^-). \quad (4.32)$$

The fixed points \hat{A}^\pm and ground states \hat{A}_0^\pm of (4.32) are then given as follows

$$\hat{A}^\pm = \frac{3}{4} \left\{ \frac{\hat{\lambda}_1}{\lambda_{\min}^2} \pm \frac{1}{\lambda_{\min}^2} \sqrt{\hat{\lambda}_1^2 - \frac{4}{3} \left(\hat{\lambda}_1^2 + \frac{\hat{\kappa}_1}{\hat{\kappa}_2} \hat{\gamma}_1 \right)} \right\}, \quad (4.33)$$

$$\hat{A}_0^\pm = \frac{1}{\lambda_{\min}^2} \left\{ \hat{\lambda}_1 \pm \sqrt{-\frac{1}{2\hat{\kappa}_2} \left(3\hat{\kappa}_1 \hat{\gamma}_1 + \hat{\kappa}_2 \hat{\lambda}_1^2 \right)} \right\}. \quad (4.34)$$

Equation (4.32) admits a localised solution if and only if the following two conditions are satisfied

$$\hat{\kappa}_1 \hat{\gamma}_1 + \hat{\kappa}_2 \hat{\lambda}_1^2 > 0, \quad 3 \hat{\kappa}_1 \hat{\gamma}_1 + \hat{\kappa}_2 \hat{\lambda}_1^2 \leq 0. \quad (4.35)$$

The first condition (4.35)₁ ensures that the localised solution decays as $|\hat{s}| \rightarrow \infty$ and that there are fixed points other than $\hat{A} = 0$, whereas (4.35)₂ guarantees that $\hat{A}' = 0$ has a non-trivial root (i.e. \hat{A}_0^- is real). We observe that (4.35) cannot be satisfied at $\hat{\lambda}_1 = 0$, and it will be shown shortly that a kink-wave solution exists in place of localisation at this point. For fixed $\hat{\gamma}_1 > 0$, as $\hat{\lambda}_1$ is increased from a sufficiently small value or decreased from a sufficiently large value, a non-trivial fixed point (a center) first becomes possible when (4.35)₁ is satisfied. Thus, as shown by the spectral interpretation previously, the greatest lower bound of (4.35)₁ is the bifurcation condition for localised bulging or necking in a small neighbourhood of $(\lambda_{\min}, \gamma_{\min})$, and should therefore be equivalent to the following two-term expansion of the original bifurcation condition (3.8)

$$\gamma = \gamma_{\min} + \frac{1}{2} (\lambda - \lambda_{\min})^2 \cdot \left. \frac{d^2 \gamma}{d\lambda^2} \right|_{\lambda=\lambda_{\min}}. \quad (4.36)$$

On substituting (4.26) into (4.36) and then comparing the resulting expression with the greatest lower bound of (4.35)₁, we obtain

$$\hat{\kappa}_2 = -\frac{1}{2} \hat{\kappa}_1 \left. \frac{d^2 \gamma}{d\lambda^2} \right|_{\lambda=\lambda_{\min}}, \quad (4.37)$$

which we have verified is numerically equivalent to (4.31) and which confirms the positivity of $\hat{\kappa}_2$ explicitly.

On combining the inequalities in (4.35), we obtain the following range of values of $\hat{\lambda}_1$ for which a localised solution can exist

$$\hat{\lambda}_1^R < |\hat{\lambda}_1| < \sqrt{3} \hat{\lambda}_1^R, \quad (4.38)$$

where $\hat{\lambda}_1^R$ is as given in (4.30). The localised solution is given explicitly in [30] as follows

$$\hat{A}(\hat{s}) = \frac{\hat{A}_0^+ \hat{A}_0^- (1 - \zeta^2)}{\hat{A}_0^+ - \hat{A}_0^- \zeta^2}, \quad \text{where} \quad \zeta(\hat{s}) = \tanh \left[-\sqrt{\frac{\hat{\kappa}_2 \hat{A}_0^+ \hat{A}_0^-}{6}} \lambda_{\min}^2 \hat{s} \right], \quad (4.39)$$

and first emerges sub-critically as $|\hat{\lambda}_1| \rightarrow \hat{\lambda}_1^R$. In the limit $|\hat{\lambda}_1| \rightarrow \sqrt{3} \hat{\lambda}_1^R$, (4.39) degenerates into a kink-wave solution characterised by two regions of uniform but distinct axial stretch connected by a smooth transition region. Further insights into this bifurcation process will be provided in section 6.

(b) Taking γ as the control parameter with λ fixed

An alternate approach is to subject the tube to a fixed axial stretch λ initially and then increase the surface tension monotonically from zero. Varying the surface tension can be achieved chemically by lowering the shear modulus of the material through temperature change, say. We set

$$\gamma = \gamma_{\text{cr}} + \varepsilon \tilde{\gamma}_1, \quad (4.40)$$

where $\tilde{\gamma}_1$ is a constant of $O(1)$ and the bifurcation values γ_{cr} satisfy (3.8) with λ_{cr} replaced by a fixed λ on the right-hand side. Then, by applying the same solution procedure as presented in the previous section, we obtain the following amplitude equation

$$\mathcal{A}'' = \tilde{\gamma}_1 \tilde{\kappa}_1 \mathcal{A} + \tilde{\kappa}_2 \mathcal{A}^2, \quad (4.41)$$

whose solitary wave solution is equivalent to (4.23) but with λ_1 replaced by $\tilde{\gamma}_1$ and $\kappa_{1,2}$ replaced by $\tilde{\kappa}_{1,2}$. The coefficient $\tilde{\kappa}_1$ is equivalent to (4.29), but with the right hand side evaluated at the fixed λ rather than λ_{\min} . Thus, unlike its counterpart κ_1 in the previous loading scenario, $\tilde{\kappa}_1$ is generally negative. This can be justified through a spectral interpretation analogous to that

presented in Fig. 9. In this loading scenario, the non-trivial eigenvalues are $\pm\alpha_1 = \pm\sqrt{\tilde{\gamma}_1 \tilde{\kappa}_1}$. Since for *any* fixed λ the constant $\tilde{\gamma}_1$ is negative (resp. positive) in the sub-critical (resp. super-critical) regime, we require that $\tilde{\kappa}_1 < 0$ for the expected exponential (resp. periodic) behaviour to occur. Based on the findings for a solid cylinder [30], we expect that the relation $\tilde{\kappa}_2 = \lambda^2 \tilde{\kappa}_1 d\gamma_{cr}/d\lambda$ holds true, and we have verified this numerically for the Gent material model. The localised solitary wave solution to (4.41) then corresponds to necking for $\tilde{\kappa}_2 > 0$ and bulging for $\tilde{\kappa}_2 < 0$, and both of these occur sub-critically since $\tilde{\gamma}_1$ must necessarily be negative. Unlike in the previous case, both the necking and bulging solutions are of practical interest here since we may feasibly fix $\lambda < \lambda_{\min}$ or $\lambda > \lambda_{\min}$.

In the limit $\lambda \rightarrow \lambda_{\min}$, $\tilde{\kappa}_2$ vanishes and the solitary wave solution diverges. Through appropriate re-scaling of \mathcal{A} , the amplitude solution (4.39) is found to be valid in this limiting case also. However, the interpretation of the bifurcation behaviour here is different to the previous loading scenario, and this latter point will be made clear in the next section.

5. Further interpretation of the bifurcation process

Although we have explicitly classified the range of bifurcation behaviours that can exist in the near critical regime, the task of interpreting the actual *observable* deformation that the tube goes through still remains. Here we give a detailed exposition of the actual post-bifurcation solution that experimentalists can expect to observe in Case 2, and it is hoped that this will be beneficial in future studies. This analysis is fully supported by previous FEM simulations [30,45].

(a) Taking λ as the control parameter with γ fixed

In this loading scenario, we apply a fixed surface tension $\gamma = \gamma_0$ with zero axial force initially. As was shown previously in Fig. 4 (b), this produces an initial axial stretch $\lambda < 1$ which we then increase from in a controlled and gradual manner. At this point we refer the reader to Fig. 9, which supplements the following interpretations.

We assume initially that γ_0 is greater than γ_{\min} by some amount of $O(\varepsilon^2)$. As λ is increased, we move horizontally in the direction of the arrow shown, and prior to $\hat{\lambda}_1 \rightarrow \sqrt{3}\hat{\lambda}_1^L$ (i.e. before we reach the left-most red dot), the tube expectedly admits the primary axial tension deformation given in section 3. However, when we attain this limit, bifurcation into a fully developed kink-wave solution does not yet occur. To elaborate, a direct transition from the primary axial tension state to a "two-phase" deformation can only be expected to occur if the perturbations applied to the tube are large in amplitude [51]. Given that our axial loading is extremely controlled, such a bifurcation is not feasible. In fact, bifurcation does not occur until $\hat{\lambda}_1 \approx \hat{\lambda}_1^L$ (as indicated by the black dot), and the associated solution is a localised neck of *infinitesimal* amplitude. At this point of bifurcation, we fix the axial length $\ell_0 = \lambda_0 L$, and we synonymously define the quantity $\lambda = \lambda_0$ as the *averaged axial stretch* (i.e. the ratio of the total deformed to undeformed length of the tube). Indeed, λ_0 depends on the choice of γ_0 , and the former is equivalently the axial stretch at $|z| \rightarrow \infty$ at the point of bifurcation. Given some small amplitude *environmental* perturbation, the monotonic growth of the necking solution to a *near* maximum amplitude state will occur in tandem with a monotonic reduction in \mathcal{N} towards a *propagation value*. In reality, neither of these limits can be achieved, since their attainment corresponds to the emergence of a heteroclinic solution which may only exist on an infinite domain. Indeed, the *propagation value* is more commonly referred to as the *Maxwell state* which indicates the emergence of the fully developed "two-phase" deformation described previously. Now, based on experimental results for the analogous problem of localisation in tubes under internal inflation [52], we expect that the necking solution is highly unstable, and that the reduction of \mathcal{N} towards the Maxwell state after the initial bifurcation takes place will consequently be rapid. Then, a similarly rapid axial propagation of the neck will occur, culminating in a final "two-phase" deformation configuration. In essence, the localised solution attained at $\lambda = \lambda_0$ will *jump* to the "two-phase", depressed kink

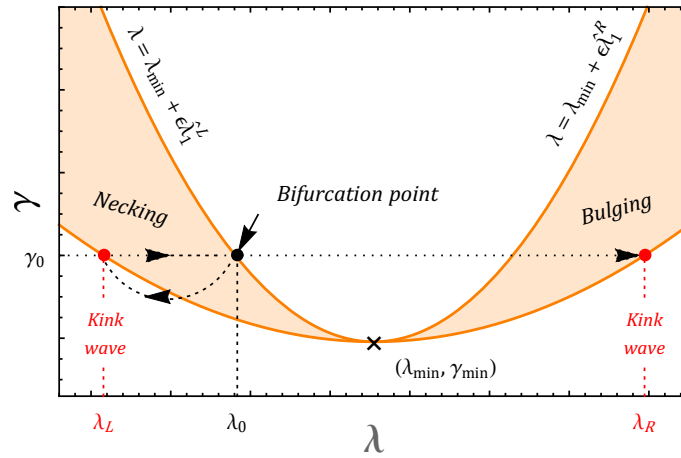


Figure 9: (Colour online) A plots of the interval (4.38) in which a localised bifurcation can actually occur (orange region) in the vicinity of $(\lambda_{\min}, \gamma_{\min})$ for a representative case $A = 0.4$. On fixing $\gamma = \gamma_0 > \gamma_{\min}$ with $\mathcal{N} = 0$ initially, an axial stretch $\lambda < \lambda_{\text{cr}}^L$ is produced. As we increase λ monotonically, we move along the arrow shown from left to right. Bifurcation into a localised *necking* solution occurs once $\hat{\lambda}_1 \approx \hat{\lambda}_1^L$ (as shown by the black dot), and we fix the stretch at this bifurcation value thereafter. A *jump* to the two red dots then occurs. This corresponds to the rapid growth and propagation of the neck into a kink-wave solution whose two "phases" have the stretches $\lambda_{L,R}$, with the average axial stretch remaining fixed at the bifurcation value λ_0 .

wave solution at the left and right red dots in Fig. 9. The total average axial stretch of this two-phase deformation configuration is $\lambda = \lambda_0$ as previously stated, but it consists of a depressed region centred at $z = 0$ with $\lambda = \lambda_R > \lambda_0$ in between two bulged regions with $\lambda = \lambda_L < \lambda_0$. For any γ_0 greater than γ_{\min} by $O(\varepsilon^2)$, we have from the interval (4.38) that

$$\lambda_{L,R} = \lambda_{\min} + \sqrt{3}\varepsilon \hat{\lambda}_1^{L,R}. \quad (5.1)$$

The axial length of the necking "phase" ℓ_{neck} is then simply defined through $\ell_{\text{neck}}/\ell_0 = |1 - \lambda_L/\lambda_0|$. We note that, in defining ℓ_{neck} , we are assuming that the axial length of the smooth transition region joining the two phases is negligible. Notably, where $\gamma_0 = \gamma_{\min}$, we have that $\lambda_{L,R} = \lambda_{\min}$ by (5.1), meaning that at the point of bifurcation the tube maintains its primary state since the two "phases" are identical.

Away from $(\lambda_{\min}, \gamma_{\min})$, analytical solutions for $\lambda_{L,R}$ are no longer possible, but we can use the Maxwell construction to generalise the previous interpretations. Maxwell's equal area rule states that the stretches $\lambda_{L,R}$ must satisfy the relations

$$S_{zz}(\lambda_L) = S_{zz}(\lambda_R) \quad \text{and} \quad \int_{\lambda_L}^{\lambda_R} S_{zz} d\lambda = S_{zz}(\lambda_L)(\lambda_R - \lambda_L), \quad (5.2)$$

where $S_{zz} = \mathcal{N}/\pi(1 - A)^2$ is the nominal axial stress. From (5.2), we can determine numerically defined functions $\lambda_{L,R} = \lambda_{L,R}(\gamma)$ with the aid of the *NIntegrate* command in Mathematica. Using these functions, we are able to plot in Fig. 10 the necking proportion $\ell_{\text{neck}}/\ell_0$ for several fixed γ , tube thickness's and extensibility limits. We see that the proportion of the necking phase with respect to the overall fixed length of the tube increases with γ and also with the tube thickness and extensibility limit.

If we instead attach a dead load to an end of the tube such that the starting value of λ is greater than λ_{\min} , and then gradually unload the tube from this point, bifurcation into a localised *bulging* solution will occur sub-critically. As before, a jump to a kink-wave solution follows, except in this

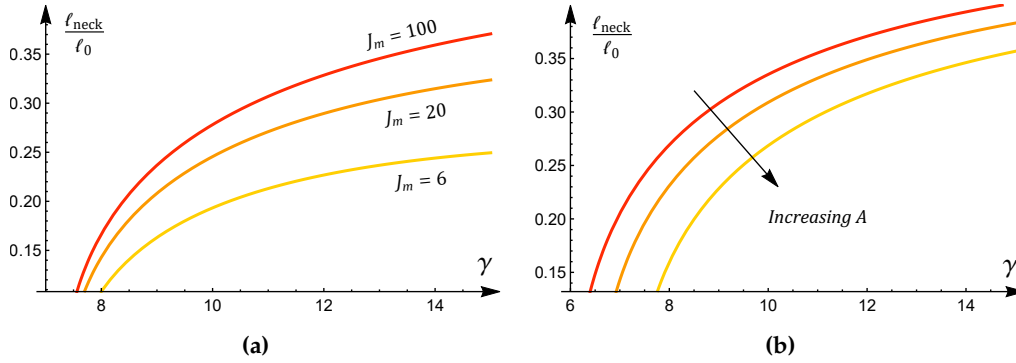


Figure 10: (Colour online) The variation of $\ell_{\text{neck}}/\ell_0$ at the point of bifurcation with respect to γ for **(a)** $A = 0.4$ and $J_m = 6, 20$ and 100 , and **(b)** $J_m = 50$ and $A = 0.2, 0.3$ and 0.4 .

case the bulged "phase" with stretch λ_R is centred at $z = 0$ and the depressed "phase" with stretch λ_L is situated at both ends.

(b) Taking γ as the control parameter with λ fixed

In this loading scenario, we assume that the *averaged axial stretch* λ_0 is fixed both before and after bifurcation takes place, with $\gamma = 0$ initially. We then increase the surface tension monotonically from zero in a gradual and controlled manner. As an illustrative example, we fix $\lambda_0 = \lambda_{\min} + \varepsilon^{1/2} \hat{\lambda}_1 > \lambda_{\min}$ initially.

Given the controlled nature in which γ is increased, bifurcation does not take place until $\hat{\gamma}_1 \approx -\hat{\kappa}_2 \hat{\lambda}_1^2 / \hat{\kappa}_1$. The associated solution is a localised *bulge* (since $\lambda_0 > \lambda_{\min}$). However, as soon as γ is increased beyond the bifurcation point, the bulge will jump to a kink-wave solution consisting of a bulged "phase" centred at $z = 0$ with axial stretch $\lambda_L < \lambda_0$ and two depressed "phases" either side with axial stretch $\lambda_R > \lambda_0$ [45]. In a small neighbourhood of λ_{\min} , the stretches $\lambda_{L,R}$ can be evaluated through

$$\lambda_{L,R} = \lambda_{\min} \mp \varepsilon^{1/2} \sqrt{-3 \hat{\gamma}_1 \hat{\kappa}_1 / \hat{\kappa}_2}, \quad \text{with} \quad \gamma = \gamma_{\min} + \varepsilon \hat{\gamma}_1. \quad (5.3)$$

Indeed, if $\lambda_0 < \lambda_{\min}$, this process would be the same, however the localised solution would instead be *necking*, and the kink-wave solution would instead be depressed about $z = 0$.

In the special case when $\lambda_0 = \lambda_{\min}$, we have already established that the solution (4.39) cannot capture the bifurcation behaviour at $\gamma = \gamma_{\min}$ since $\hat{\lambda}_1 = 0$. However, we may make the substitution $\hat{A}(\hat{s}) = 2^{-1} \lambda_{\min}^{-2} \sqrt{-3 \hat{\gamma}_1 \hat{\kappa}_1 / \hat{\kappa}_2} h(t)$, $t = \sqrt{-\hat{\gamma}_1 \hat{\kappa}_1} \hat{s}$ to reduce the amplitude equation (4.28) to $h''(t) = h(h^2 - 1)$. This latter equation has previously been derived by Xuan and Biggins [28], and it admits the kink-wave solution $h(t) = \tanh(t/\sqrt{2})$ that tends to ± 1 as $t \rightarrow \pm\infty$, respectively. The two constant "phases" corresponding to this kink-wave solution are defined through (5.3). As we increase γ beyond the associated bifurcation value γ_{\min} , a *continuous* transition to a kink-wave solution occurs, and the bifurcation is exceptionally super-critical.

6. Further insights into Case 3

In this section, we provide further insights into the possible bifurcation behaviours in Case 3. As an illustrative example, we fix $\lambda > 1 - A^2$ and take γ as the control parameter. For the sake of brevity, the neo-Hookean strain-energy is deployed here, but an extension to the Gent model can be achieved as shown previously. By applying the same approach as in section 4 (b), the

corresponding amplitude equation is determined to be of the form (4.41). The counterpart of $\tilde{\kappa}_1$ in Case 3 is still generally negative, and $\tilde{\kappa}_2 = \lambda^2 \tilde{\kappa}_1 d\gamma_{\text{cr}}/d\lambda$.

Whilst the structure of the amplitude equation appears near identical to the Case 2 counterpart, there is a subtlety which alters the interpretation of the bifurcation solutions somewhat, and this can be explained as follows. In Case 2, γ_{cr} as a function of λ has a *single* minimum for any tube thickness, as was illustrated in Fig. 3. In Case 3 however, there exists a threshold value for A below which two *additional* local extrema (i.e. a maximum and a minimum) of γ_{cr} with respect to λ emerge. For the neo-Hookean strain energy, this threshold is $A \approx 0.08567$, and in the limit $A \rightarrow 0.08567^-$ these two additional extrema of γ_{cr} coalesce to form an inflection point; see Fig. 11. Indeed, as A decreases from this threshold, the bifurcation curve will at some point intersect $\gamma_{\text{cr}} = 0$, and the range of values of λ for which localisation can occur will decrease. In the limit $A \rightarrow 0$, incompressibility may only be satisfied for $\lambda = 1$, and the associated bifurcation point $\gamma_{\text{cr}}/A \rightarrow 2$ corresponds to localisation in a cylindrical cavity surrounded by an infinite solid [22,43]. For values of A above 0.08567, the solitary wave solution corresponds to a localised neck for $1 - A^2 < \lambda < \lambda_{\text{min}}$ and a localised bulge for $\lambda > \lambda_{\text{min}}$.

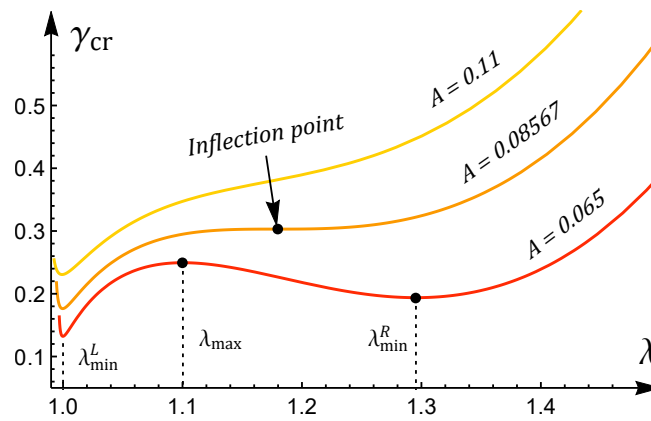


Figure 11: (Colour online) Plots of γ_{cr} against λ for $A = 0.065$ (red), $A = 0.08567$ (orange) and $A = 0.11$ (yellow). On the curve corresponding to $A = 0.065$, the black dots mark the two additional local extrema of γ_{cr} with respect to λ which emerge in the large thickness regime. In the limit $A \rightarrow 0.08567^-$, these two extrema coalesce to form an inflection point (as shown by the arrow), and above this threshold, γ_{cr} has a single minimum value.

For $A < 0.08567$, we denote by λ_{max} and $\lambda_{\text{min}}^{L,R}$ the values of λ at the maximum and the left and right hand minima of γ_{cr} . Then, given the form of $\tilde{\kappa}_2$, it follows that the localised solution in this large thickness regime corresponds to necking for $1 - A^2 < \lambda < \lambda_{\text{min}}^L$ and $\lambda_{\text{max}} < \lambda < \lambda_{\text{min}}^R$, and bulging for $\lambda_{\text{min}}^L < \lambda < \lambda_{\text{max}}$ and $\lambda > \lambda_{\text{min}}^R$. Now, in the limit $\lambda \rightarrow \lambda_{\text{min}}^{L,R}$, we find that the localised solution (4.39) and the interpretations in section 5 (b) remain valid. However, in the limit $\lambda \rightarrow \lambda_{\text{max}}$, a key difference lies in the fact that $\tilde{\kappa}_2$ is no longer positive; see (4.37). This means that, given the expansions $\gamma = \gamma_{\text{max}} + \varepsilon \hat{\gamma}_1$ and $\lambda = \lambda_{\text{max}} + \varepsilon^{1/2} \hat{\lambda}_1$, and the form of \hat{A}_0^\pm in (4.34), the inequality sign in the necessary condition (4.35)₂ for localisation is flipped. Therefore, in the vicinity of λ_{max} , the localised solution (4.39) instead exists for $|\hat{\lambda}_1| < \hat{\lambda}_1^R$, and thus occurs sub-critically. Moreover, since $\tilde{\kappa}_1$ and $\tilde{\kappa}_2$ are both negative in this limit, the form of $\hat{\lambda}_1^R$ suggests that $\hat{\gamma}_1$ should necessarily be *negative*. Then, on replacing λ_{min} with λ_{max} and taking the limit $\hat{\lambda}_1 \rightarrow 0$, the solution (4.39) reduces to the dark soliton $\hat{A} = (\sqrt{3} \hat{\lambda}_1^L / \sqrt{2} \lambda_{\text{max}}^2) \text{sech}(\sqrt{\tilde{\kappa}_1 \gamma_1} s)$. In contrast, the super-critical kink-wave solution $h(t)$ derived in section 5 (b) cannot exist at $\lambda = \lambda_{\text{max}}$ since we would require t to be purely imaginary. In Fig. 12, we present the range of $\hat{\lambda}_1$ for which localisation can exist in this limit, and also the evolution of the associated localised bulging solution as we approach $\hat{\lambda}_1 = \hat{\lambda}_1^L$. We observe that the bulging amplitude decreases and becomes more elongated

as we get closer to $\hat{\lambda}_1^L$. If we were instead approaching $\hat{\lambda}_1^R$, the solution would be a localised neck.

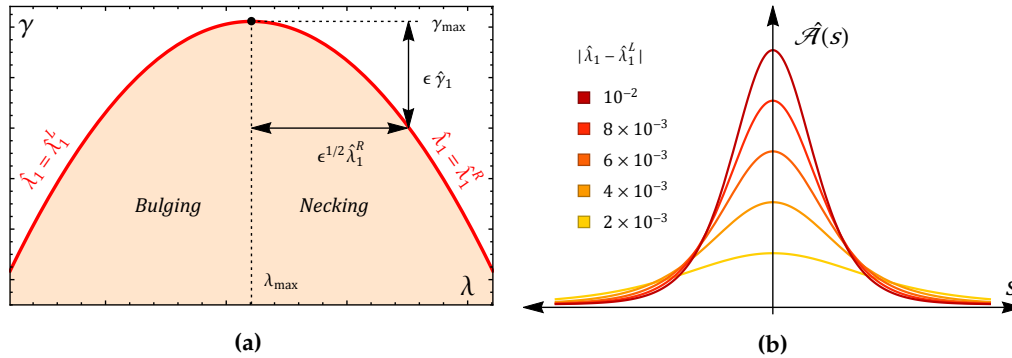


Figure 12: (a) A blow up of (3.10) in the large thickness regime about $\lambda = \lambda_{\max}$. The red curve gives the bifurcation points $\lambda = \lambda_{\max} + \epsilon^{1/2} \hat{\lambda}_1^{L,R}$ in a small neighbourhood of λ_{\max} , whilst the orange region represents $|\hat{\lambda}_1| < \hat{\lambda}_1^R$, the domain of existence of localisation in this limiting case. In (b), the evolution of the localised bulging solution near $\hat{\lambda}_1 = \hat{\lambda}_1^L$ are given for a representative case $A = 0.05$.

7. Conclusion

If one lateral surface of a soft slender tube is in smooth contact with a rigid boundary such that radial displacement and surface tension are prohibited, with the other lateral surface remaining traction-free and under surface tension, localised bifurcation solutions become widely favourable over periodic axisymmetric modes. Contrary to our original thoughts, this statement is also true when both lateral surfaces are traction-free, as has been shown in section 3, though in this case these localised solutions are preceded by elliptic circumferential buckling modes [15]. Throughout this work, we have referred to the latter scenario as Case 1, whilst Cases 2 and 3 pertain to the scenarios where the inner or outer surfaces, respectively, are radially fixed.

Through a weakly non-linear analysis formulated in terms of a general material model, we have explicitly characterised the localised solutions which bifurcate from the primary state of axial tension in Case 2. These theoretical results pertain to two common scenarios of loading: a fixed surface tension with monotonically increasing axial stretch, or a fixed averaged axial stretch with monotonically increasing surface tension. In the former scenario, the fixed surface tension γ attains a minimum γ_{\min} at the critical axial stretch $\lambda_{\text{cr}} = \lambda_{\min}$, and there consequently exists two bifurcation values $\lambda_{\text{cr}}^L < \lambda_{\min}$ and $\lambda_{\text{cr}}^R > \lambda_{\min}$ for any fixed $\gamma > \gamma_{\min}$. We explained how, on assuming that the resultant axial force \mathcal{N} is zero initially, the left bifurcation point λ_{cr}^L is always encountered first, and the associated *sub-critical* bifurcation solution is localised necking. In the latter scenario, the localised solution was found to be necking for fixed $\lambda < \lambda_{\min}$ and bulging for $\lambda > \lambda_{\min}$. In Case 3, two additional local extrema of the critical surface tension emerge in the regime of large tube thickness, meaning that necking and bulging can occur in several separate intervals of axial stretch.

In both loading scenarios, an appropriate rescaling reveals the existence of a small region either side of $\lambda = \lambda_{\min}$ wherein a variety of localised bifurcation behaviours exist. Based on recent experimental results for localisation in tubes under internal inflation, we provided a complete interpretation of these theoretical solutions in order to aid future experimental studies. We postulated that the tube will initially admit a localised homoclinic solution whose amplitude will grow rapidly towards a near maximum state. Then, an axial propagation will occur, producing

a final "two-phase" configuration consisting of a bulged and depressed region with constant but distinct axial stretches. These stretches are given analytically in the vicinity of λ_{\min} , and are determined numerically away from this threshold through Maxwell's equal area rule. These interpretations are fully supported by Finite Element Method Simulations conducted by ourselves in [45]. At $\lambda = \lambda_{\min}$, the bifurcation is exceptionally supercritical, and the corresponding kink wave solution has been derived explicitly.

This work aimed to provide fresh theoretical understanding of the elasto-capillary bifurcation behaviour of soft tubes, and it is hoped that this will provide a fertile ground for future study in this exciting and ever developing field. We conclude by noting that, as a first attempt, we have used the simplest liquid-like surface model to describe surface effect. However, more sophisticated models that take area stretch into account [53,54], or even surface stiffness into account [55], may be used.

Data Accessibility. This article has no additional data.

Authors' Contributions. **Dominic Emery and Yibin Fu:** Conceptualisation, Methodology, Software, Writing - original draft, Writing review and editing.

Competing Interests. The authors declare they have no competing interests.

Acknowledgements. The first author (Dominic Emery) acknowledges the School of Computing and Mathematics, Keele University for supporting his PhD studies through a faculty scholarship.

References

1. Wang C, Sim K, Chen J, Kim H, Rao Z, Li Y, Chen W, Song J, Verduzco R, Yu C. 2018 Soft ultrathin electronics innervated adaptive fully soft robots. *Adv. Mater.* **30**, 1706695.
2. Qiu Y, Zhang E, Plamthottam R, Pei Q. 2019 Dielectric elastomer artificial muscle: materials innovations and device explorations. *Acc. Chem. Res.* **52**, 316–325.
3. Cooke ME, Jones SW, Ter Horst B, Moiemien N, Snow M, Chouhan G, Hill LJ, Esmaeli M, Moakes RJ, Holton J et al.. 2018 Structuring of hydrogels across multiple length scales for biomedical applications. *Adv. Mater.* **30**, 1705013.
4. Saksono P, Perić D. 2006 On finite element modelling of surface tension Variational formulation and applications—Part I: Quasistatic problems. *Computat. Mech.* **38**, 265–281.
5. Javili A, Steinmann P. 2009 A finite element framework for continua with boundary energies. Part I: The two-dimensional case. *Comput. Methods Appl. Mech. Eng.* **198**, 2198–2208.
6. Liu JL, Feng XQ. 2012 On elastocapillarity: A review. *Acta Mech. Sin.* **28**, 928–940.
7. Papastavrou A, Steinmann P, Kuhl E. 2013 On the mechanics of continua with boundary energies and growing surfaces. *J. Mech. Phys. Solids* **61**, 1446–1463.
8. Liu T, Jagota A, Hui CY. 2017 A closed form large deformation solution of plate bending with surface effects. *Soft Matter* **13**, 386–393.
9. Bico J, Reyssat É, Roman B. 2018 Elastocapillarity: When surface tension deforms elastic solids. *Annu. Rev. Fluid Mech.* **50**, 629–659.
10. Style RW, Jagota A, Hui CY, Dufresne ER. 2017 Elastocapillarity: Surface tension and the mechanics of soft solids. *Ann. Rev. Cond. Matter. Phys* **8**, 99–118.
11. Shyer AE, Tallinen T, Nerurkar NL, Wei Z, Gil ES, Kaplan DL, Tabin CJ, Mahadevan L. 2013 Villification: how the gut gets its villi. *Science* **342**, 212–218.
12. Seow CY, Wang L, Paré PD. 2000 Airway narrowing and internal structural constraints. *J. Appl. Physiol.* **88**, 527–533.
13. Balbi V, Destrade M, Goriely A. 2020 Mechanics of human brain organoids. *Phys. Rev. E* **101**, 022403.
14. Hazel AL, Heil M. 2005 Surface-tension-induced buckling of liquid-lined elastic tubes: a model for pulmonary airway closure. *Proc. R. Soc. A.* **461**, 1847–1868.
15. Emery DR, Fu YB. 2021 Elasto-capillary circumferential buckling of soft tubes under axial loading: existence and competition with localised beading and periodic axial modes. *Mech. Soft Mater.* **3**. doi: <https://doi.org/10.1007/s42558-021-00034-x>.
16. Riccobelli D, Bevilacqua G. 2020 Surface tension controls the onset of gyrification in brain organoids. *J Mech Phys Solids* **134**, 103745.
17. Wang Q, Liu M, Wang Z, Chen C, Wu J. 2021 Large deformation and instability of soft hollow cylinder with surface effects. *J. Appl. Mech.* **88**.

18. Barrière B, Sekimoto K, Leibler L. 1996 Peristaltic instability of cylindrical gels. *J. Chem. Phys.* **105**, 1735–1738.
19. Mora S, Phou T, Fromental JM, Pismen LM, Pomeau Y. 2010 Capillarity driven instability of a soft solid. *Phys. Rev. Lett.* **105**, 214301.
20. Ciarletta P, Amar MB. 2012 Peristaltic patterns for swelling and shrinking of soft cylindrical gels. *Soft Matter* **8**, 1760–1763.
21. Taffetani M, Ciarletta P. 2015 Beading instability in soft cylindrical gels with capillary energy: weakly non-linear analysis and numerical simulations. *J. Mech. Phys. Solids* **81**, 91–120.
22. Xuan C, Biggins J. 2016 Finite-wavelength surface-tension-driven instabilities in soft solids, including instability in a cylindrical channel through an elastic solid. *Phys. Rev. E* **94**, 023107.
23. Lestringant C, Audoly B. 2020 A one-dimensional model for elasto-capillary necking. *Proc. R. Soc. Lond. A* **476**, 20200337.
24. Bar-Ziv R, Moses E. 1994 Instability and "pearling" states produced in tubular membranes by competition of curvature and tension. *Phys. Rev. Lett.* **73**, 1392.
25. Kilinc D, Gallo G, Barbee KA. 2009 Interactive image analysis programs for quantifying injury-induced axonal beading and microtubule disruption. *Comp. Meth. Progr. Biom* **95**, 62–71.
26. Goriely A, Geers MG, Holzapfel GA, Jayamohan J, Jérusalem A, Sivaloganathan S, Squier W, van Dommelen JA, Waters S, Kuhl E. 2015 Mechanics of the brain: perspectives, challenges, and opportunities. *Biomech. Model. Mechanobiol* **14**, 931–965.
27. Datar A, Ameeramja J, Bhat A, Srivastava R, Mishra A, Bernal R, Prost J, Callan-Jones A, Pullarkat PA. 2019 The roles of microtubules and membrane tension in axonal beading, retraction, and atrophy. *Biophys. J.* **117**, 880–891.
28. Xuan C, Biggins J. 2017 Plateau-Rayleigh instability in solids is a simple phase separation. *Phys. Rev. E* **95**, 053106.
29. Giudici A, Biggins JS. 2020 Ballooning, bulging and necking: an exact solution for longitudinal phase separation in elastic systems near a critical point. *Phys. Rev. E* **102**, 033007.
30. Fu YB, Jin L, Goriely A. 2021 Necking, beading, and bulging in soft elastic cylinders. *J. Mech. Phys. Solids* **147**, 104250.
31. Ménager C, Meyer M, Cabuil V, Cebers A, Bacri JC, Perzynski R. 2002 Magnetic phospholipid tubes connected to magnetoliposomes: pearling instability induced by a magnetic field. *Eur. Phys. J. E* **7**, 325–337.
32. Tsafirir I, Sagi D, Arzi T, Guedeau-Boudeville MA, Frette V, Kandel D, Stavans J. 2001 Pearling instabilities of membrane tubes with anchored polymers. *Phys. Rev. Lett.* **86**, 1138.
33. Hannezo E, Prost J, Joanny JF. 2012 Mechanical instabilities of biological tubes. *Phys. Rev. Lett.* **109**, 018101.
34. Ma L, Peng J, Wu C, He L, Ni Y. 2017 Sphere-to-tube transition toward nanotube formation: a universal route by inverse plateau-rayleigh instability. *ACS nano* **11**, 2928–2933.
35. Shimizu T, Ding W, Kameta N. 2020 Soft-matter nanotubes: a platform for diverse functions and applications. *Chem. Rev.* **120**, 2347–2407.
36. Rustom A, Saffrich R, Markovic I, Walther P, Gerdes HH. 2004 Nanotubular highways for intercellular organelle transport. *Science* **303**, 1007–1010.
37. Schara K, Janša V, Šuštar V, Dolinar D, Pavlič JI, Lokar M, Kralj-Iglič V, Veranič P, Iglič A. 2009 Mechanisms for the formation of membranous nanostructures in cell-to-cell communication. *Cell. Mol. Biol. Lett.* **14**, 636–656.
38. Sisakhtnezhad S, Khosravi L. 2015 Emerging physiological and pathological implications of tunneling nanotubes formation between cells. *Eur. J. Cell Biol.* **94**, 429–443.
39. Vignais ML, Caicedo A, Brondello JM, Jorgensen C. 2017 Cell connections by tunneling nanotubes: effects of mitochondrial trafficking on target cell metabolism, homeostasis, and response to therapy. *Stem Cells Int.* **2017**.
40. Drab M, Stopar D, Kralj-Iglič V, Iglič A. 2019 Inception mechanisms of tunneling nanotubes. *Cells* **8**, 626.
41. Alimohamadi H, Ovryn B, Rangamani P. 2020 Modeling membrane nanotube morphology: the role of heterogeneity in composition and material properties. *Sci. Rep.* **10**, 1–15.
42. Veranič P, Lokar M, Schütz GJ, Weghuber J, Wieser S, Hägerstrand H, Kralj-Iglič V, Iglič A. 2008 Different types of cell-to-cell connections mediated by nanotubular structures. *Biophys. J.* **95**, 4416–4425.
43. Henann DL, Bertoldi K. 2014 Modeling of elasto-capillary phenomena. *Soft Matter* **10**, 709–717.
44. Wang L. 2020 Axisymmetric instability of soft elastic tubes under axial load and surface tension. *Int. J. Solids. Struct.* **191**, 341–350.

45. Emery D, Fu Y. 2021 Localised bifurcation in soft cylindrical tubes under axial stretching and surface tension. *Int. J. Solids Struct.* **219**, 23–33.
46. Ye Y, Liu Y, Fu YB. 2020 Weakly nonlinear analysis of localized bulging of an inflated hyperelastic tube of arbitrary wall thickness. *J. Mech. Phys. Solids* **135**, 103804.
47. Wineman A. 2005 Some results for generalized neo-Hookean elastic materials. *Int. J. Non-Linear Mech.* **40**, 271–279.
48. Ciarletta P. 2011 Generating functions for volume-preserving transformations. *Int. J. Non-Linear Mech* **46**, 1275–1279.
49. Wolfram Research Inc.. 2019 *Mathematica 12.0*. Wolfram Research Inc, Champaign, IL.
50. Fu YB. 2001 Nonlinear stability analysis. In Fu YB, Ogden RW, editors, *Nonlinear elasticity: Theory and Applications*. Cambridge: Cambridge University Press.
51. Ericksen JL. 1975 Equilibrium of bars. *J. Elast.* **5**, 191–201.
52. Wang S, Guo Z, Zhou L, Li L, Fu Y. 2019 An experimental study of localized bulging in inflated cylindrical tubes guided by newly emerged analytical results. *J. Mech. Phys. Solids* **124**, 536–554.
53. Gurtin ME, Murdoch AI. 1975 A continuum theory of elastic material surfaces. *Arch. Ration. Mech. Anal.* **57**, 291–323.
54. Huang Z, Wang Jx. 2006 A theory of hyperelasticity of multi-phase media with surface/interface energy effect. *Acta Mech.* **182**, 195–210.
55. Steigmann D, Ogden R. 1997 Plane deformations of elastic solids with intrinsic boundary elasticity. *Proc. R. Soc. A* **453**, 853–877.